

Development of Compact Fluorescence Spectrometers and Field Deployable Optical Solids Content  
Monitoring Devices

by

Timothy Then-Siong Ho

A thesis submitted in partial fulfillment of the requirements for the degree of

Master of Science

in Photonics and Plasmas

Department of Electrical and Computer Engineering  
University of Alberta

© Timothy Then-Siong Ho, 2014

## **Abstract**

Two techniques were used to develop industrial and environmental sensing devices: fluorescence spectrometry and light scatter. The focus of the thesis is to develop real-time, portable and economical sensors using these techniques for environmental detection and management of tailings slurries. A compact fluorescence spectrometer compatible with cone penetration was developed for hydrocarbon contamination in soils. To be compatible, the device was designed to fit into a 25 mm diameter tube. To simplify the alignment of optics in a small space, 5 long-pass filters were used to divide the fluorescence spectrum for spectral analysis. A 405 nm wavelength laser diode was used as the excitation source because of its high output, sufficiently high photon energy and cost-effectiveness. Fluorescence results were obtained and show capability to differentiate between several fluorescence spectra.

The light scatter intensity of highly concentrated slurries, typically 30% w/w to 70% w/w, was investigated using blue (405 nm wavelength) and red (639 to 650 nm wavelengths) laser diodes. First, a small test cylinder was used to learn about the relationship between light scattered and solids content of a sample. A ring device was also constructed for use with cuvettes to analyse the angular distribution of the light scatter and light scatter intensity for various samples including different tailings slurries and polystyrene beads. This ring was also used to develop a calibration relationship between solids content and relative amount of light scattered. Using the relationship established, 3 different sensor systems were developed under differing criteria to measure concentration (or solids content) of slurries undergoing 3 methods of dewatering. A centrifuge sensor was made to withstand 100 times gravity and measure in real time. A 3 m tall device was built to continuously monitor the progress of tailings with flocculants settling over the course of a year. Finally, a sensor was designed to measure changing solids content of slurries being actively processed in a pipeline, using a credit-card sized economical microprocessor as the main

computation device. These three devices were field tested and show light scatter sensitivity to the changing solids content.

## **Preface**

The Design and Analysis Method sections of Chapter 3 were published as T. T. Ho, M. Gupta, M. T. Taschuk, M. Alostaz, A. Ulrich, D. C. Segó, R. Dolling, D. Woeller and Y. Y. Tsui, "Fluorescence Spectrophotometer for Cone-Penetrometer Applications," in *Third International Oil Sands Tailings Conference*, Edmonton, Alberta, 2012. I was responsible for device construction, data collection and analysis, and manuscript composition. M. Gupta assisted with the device construction and data collection. All authors contributed to manuscript editing. Y. Y. Tsui was the supervisory author and was also involved with the conception of the project. Additional experiments, including refinements to the analysis, and subsequent results carried out after this publication, shown in Chapter 3, are my original work.

Portions of the Stationary Cylinder and Centrifuge Sensor sections of Chapter 4 were published as M. Gupta, Y. Zhou, T. T. Ho, A. Sorta, M. T. Taschuk, D. C. Segó and Y. Y. Tsui, "Solid Content of Oil Sands Tailings Measured Optically," in *Third International Oil Sands Tailings Conference*, Edmonton, Alberta, 2012. I was responsible for device construction, data collection and analysis of results shown in this thesis. Y. Zhou was responsible for the data collection and analysis of the plots shown in Figure 4-1. M. Gupta assisted with data collection and analysis and was responsible for manuscript composition and all authors contributed to manuscript editing. Y. Y. Tsui was the supervisory author and was also involved with the conception of the project.

## **Acknowledgements**

First and foremost, thank you to my advisor Professor Ying Tsui for interesting projects, constant guidance and helpful nudges in the right direction starting back in my undergraduate capstone project. This thesis would not have been possible without his support and help developing all the necessary skills. Also thanks to Dr. Manisha Gupta, whom I worked with on several projects, and to all of my labmates for all manner of random help: Fatema Chowdhury, Hesam Shahim, Mei Shen, Zhijiang Chen, Debbie Ha and Yu (Carol) Zhou.

All of these devices exist in the real world because of the ECE machine shop who built all of the bits and parts. Thank you to Herbert Dixel and the machinists for all the helpful discussions, and for making all the edits and modifications which brought these devices into reality.

Finally, I would like to thank my family and friends for their endless support, listening to my crazy ideas, and for keeping the other half of life exciting.

Financial support for this work was provided by the Natural Sciences and Engineering Research Council (NSERC), Alberta Innovates Technology Futures (AITF) and the University of Alberta.

# Table of Contents

1.	Introduction:.....	1
1.1	Fluorescence:.....	3
1.2	Spectrometer:.....	3
1.3	Cone Penetration:.....	3
1.4	Chemicals of Interest.....	4
1.5	Laser Diodes: .....	4
1.6	Light Scatter:.....	5
1.7	Description of Project:.....	5
2.	Theory:.....	7
2.1	Fluorescence:.....	7
2.2	Light Scatter:.....	8
2.3	Settling:.....	11
3.	Fluorescence Spectrometer .....	13
3.1	Previous Work .....	13
3.2	Design .....	14
3.3	Analysis method .....	15
3.4	Results .....	17
3.5	Discussion .....	19
3.6	Field Test Design:.....	23
3.7	Summary.....	24
4.	Light Scatter Sensors: .....	26
4.1	Stationary Cylinder: .....	27
4.1.1	Design .....	27
4.1.2	Results: .....	30
4.2	Calibration Ring: .....	33

4.2.1	Design: .....	33
4.2.2	Kaolin & Tailings: .....	34
4.2.3	Flow Sensor Sample:.....	36
4.2.4	Polystyrene Beads: .....	37
4.3	Centrifuge Sensor: .....	39
4.3.1	Design: .....	39
4.3.2	Testing & Results: .....	40
4.3.3	Summary.....	42
4.4	Insertion Sensor:.....	43
4.4.1	Design .....	43
4.4.2	Initial Testing .....	46
4.4.3	Results & Analysis:.....	47
4.4.4	Summary.....	51
4.5	Flow Sensor: .....	52
4.5.1	Design .....	52
4.5.2	Results .....	56
4.5.3	Summary.....	57
5.	Summary & Future Directions .....	58
6.	Bibliography.....	60
	Appendix A: Schematics for Devices .....	63
	Centrifuge Sensor .....	63
	Insertion Sensor.....	63
	Flow Sensor .....	64
	Appendix B: Flow Sensor Circuit Diagram .....	65
	Appendix C: Software .....	67
	Insertion Sensor.....	67

Flow Sensor ..... 67

## List of Tables

Table 3-1 – Fluorescence efficiency @ 405 nm.....	22
---	----

## List of Figures

Figure 2-1 – Schematic of light scattering geometry. The scattering angle is measured with respect to the direction of unimpeded light. ....	8
Figure 2-2 – Scatter intensity calculated with MiePlot program for a single scatterer at 160° and 405 nm wavelength. The scatter intensity increases in general with particle diameter. Rayleigh particle size region is labeled and Mie region shows more complicated effects. ....	9
Figure 2-3 – Plot showing the scatter intensity in relation to the solids content. Three regions occur for dilute, concentrated and highly concentrated particles. ....	10
Figure 3-1 – Schematic of setup. Excitation source in center of ‘filter wheel’ is focussed by the parabolic mirror onto sample area. Fluoresced light is collected by the parabolic mirror, passes through filters and is focussed onto imaging CCD. [3] .....	14
Figure 3-2 – Transmission spectra of 5 filters used. Lower right: image of the filter wheel; middle location will hold excitation laser diode. Upper right: sample image captured from device. Colour available in electronic version. ....	14
Figure 3-3 – Pyrene fluorescence spectra. Laser diode excitation peak (405nm) and effects of each filter shown. Measured and calculated spectra (red, green) are well matched. Colour available in electronic version. ....	15
Figure 3-4 – Top: Orange fluorescent paper; Bottom: Green fluorescent paper. Colour available in electronic version.....	17
Figure 3-5 – Polycyclic hydrocarbons in clay. Concentration of 21, 34 and 69 parts per thousand for naphthalene, phenanthrene and pyrene respectively. Colour available in electronic version.....	18
Figure 3-6 – Comparison of crude oil and MFT fluorescence with 405 nm excitation. Crude oil concentration of $6.3 \times 10^{-3}$ and bitumen concentration in MFT $17 \times 10^{-3}$ . Colour available in electronic version.....	19
Figure 3-7 – Fluorescence signal from diesel and gasoline @405 nm excitation. Colour available in electronic version.....	21
Figure 4-1 – Scatter signal measured with changing solid content % for (a) Kaolin, (b) Gold tailings, (c) Devon silt, (d) TUT, (e) AL15, and (f) AL7.5. Kaolin, Gold tailings and Devon show increase in signal with increasing solids content, but the MFT (d – f) show a somewhat reverse trend. [2] .....	26

Figure 4-2 – Schematic of laser diode and photodiode arrangement. There is a 20° angle between the laser diode and photodiode, and they are spaced 1 cm apart vertically. .... 27

Figure 4-3 – Laser pulsing circuit. Top left: voltage regulator; bottom left: square pulse generator; right: laser driver IC..... 28

Figure 4-4 – Schematic of beam-splitter design. Laser diode emits downward and the beam-splitters redirect a part of the beam horizontally..... 29

Figure 4-5 – Example setup with TUT % sample. Left side, top to bottom CH1, CH4, CH6 and right side CH2. .... 30

Figure 4-6 – Kaolin 33% starting solids content of hours elapsed versus relative signal strength. Measurement heights at 18 cm, 15.5cm, 10.5 cm and 1 cm for CH1 through CH6 respectively and measurement angle was at 20° backscatter. .... 31

Figure 4-7 – TUT 35% starting solids content measured over 23 day settling. Measurement heights at 18 cm, 15.5cm, 10.5 cm and 1 cm for CH1 through CH6 respectively and measurement angle was at 20° backscatter. Two gaps in data are due to an error in data collection trigger and a power outage. .... 32

Figure 4-8 – A microscope picture taken of Kaolin powder showing range of particle sizes and irregularity of shape..... 33

Figure 4-9 – Calibration ring setup. Focussed laser diode enters at 12 o'clock on this schematic and 4 detectors are positioned on either side of the laser diode. .... 34

Figure 4-10 – Light scatter signal change depending on angle for different solid content mixtures of Kaolin. The source used was a 405 nm wavelength laser diode. .... 35

Figure 4-11 – Kaolin calibration measured at 20° backscatter and 405 nm source. Various concentrations were made and measured to find the relative change in signal with solids content. The shape of the plot is typical for both Kaolin and various tailings samples. .... 35

Figure 4-12 - Measurement of the backscatter signal at 20° with 405 nm wavelength source of sandy sample diluted in saturated salt solution. Samples at 90% and 100% did not have enough water to be fully wetted. .... 36

Figure 4-13 – Light scatter from various diameters of polystyrene beads in 0.1% w/w aqueous solution, measured at 20° backscatter with 405 nm wavelength source. .... 37

Figure 4-14 – Centrifuge sensor. Signal amplifiers on perforated board at left, and laser diode driver on perforated board at top. Detectors covered by bandpass filters at center, and glass beam splitters at right..... 39

Figure 4-15 – Device test verifying the performance of the sensor using 405 nm wavelength source and measuring at 20°. The neighbouring detectors interfere with the signal..... 40

Figure 4-16 – Normalised signal of MFT in centrifuge run at 60g. Light signal decreases to around 0.6 once the solids have settled below that level and water remains. The solids settle below the first 3 levels after 50 hours. Colour available in electronic version. .... 41

Figure 4-17 – Schematic of the sensor. The PC is connected with the sensors though USB hubs and controls the laser driver card. Signals from the sensors are amplified and then read by the data acquisition (DAQ) into the software to be logged and plotted..... 43

Figure 4-18 – Electronics box containing laser driver, data acquisition and signal amplifiers. Power input screw terminals are mounted outside the box on the left. Slots have been cut on the left and right sides to allow wiring to exit the box. .... 44

Figure 4-19 – Thickener Feed without flocculent. Schematic on the left shows the relative locations of the sensors and corresponds with the adjacent signals on the graph to the right. Colour available in electronic version..... 46

Figure 4-20 – Comparison of the window clarity a) before use, b) right after removal from the tank, and c) after rinsing with water..... 47

Figure 4-21 – Calibration curve for the MFT tested in the settling tank at 20° backscatter. The 0% for the blue laser is high because of small particulates which do not settle out. Colour available in electronic version. .... 47

Figure 4-22 – Comparison of the gamma ray sensor and samples drawn from the tank, measured with gravimetric method (oven drying) and light scatter (calibration ring). The light scatter is signal fit to the gravimetric measurement. Colour available in electronic version..... 48

Figure 4-23 – Blue sensor data for 4 heights in the tank. The upper two sensors eventually reach ‘water’ whereas the lower two sensor remain in solids. Colour available in electronic version..... 49

Figure 4-24 – Clear section on the upper part of the window after the tube was removed. This is possibly caused by air bubbles, which may have affected measurements from the red laser diodes. .... 50

Figure 4-25 – (a) The sensors are placed at the supply and return of the sample tank. (b) The detector setup has two laser diodes flanking a photodiode detector above the sampling window. Light scatter is collected at a 20° angle..... 52

Figure 4-26 – Flow sensor electronics. Raspberry Pi and power supply at right and at left breadboard circuitry for amplifying, sending, and reading signals. .... 53

Figure 4-27 – A comparison of data between light scatter measurements and the sample’s density. Normalized light scatter signal (measured at 20°) shown above and below the measured density of the slurry. .... 56

## List of Abbreviations

MFT.....	Mature fine tailings
s.c.....	Solids content
CPT.....	Cone penetration
NA.....	Naphthenic Acid
CCD.....	Charge-coupled Device
UV.....	Ultraviolet
LED.....	Light Emitting Diode
EEM.....	Excitation-emission Matrix
w/w.....	weight per weight
USB.....	Universal Serial Bus
NIR.....	Near Infrared
FWHM.....	Full Width, Half Maximum
CMOS.....	Complementary Metal-oxide-semiconductor
TUT.....	Thickened Underflow Tailings
PVC.....	Polyvinyl Chloride
DAQ.....	Data Acquisition Card
v/v.....	volume per volume
w/v.....	weight per volume
op-amp.....	operational amplifier
PCB.....	Printed Circuit Board
GUI.....	Graphical User Interface
I/O.....	Input/Output
RPi.....	Raspberry Pi
GPIO.....	General Purpose Input/Output
ADC.....	Analog to Digital Converter
SPI.....	Serial Peripheral Interface

PWM .....Pulse Width Modulated  
MOSFET .....Metal-oxide-semiconductor Field Effect Transistor  
PI.....proportional-integral  
UART .....Universal Asynchronous Receiver/Transmitter

## **1. Introduction:**

The development of industry has greatly improved the standard of living and availability of luxuries to the general population over the past few centuries. In particular oil provides for electricity, heat, petrol, and plastics which are used in everything from toys, furniture, medical devices, pharmaceuticals, glasses and chasses for nearly anything. However, extraction and refining of oil and other industrial processes can have many chemical by-products which are hazardous to both human health and the environment. As production and development continues, care must be taken to monitor the air, land, and water to minimize pollution and contamination, and properly deal with any resulting waste. Traditionally, testing was carried out by bringing a sample from the site back to a lab for analysis, but this is not efficient for remote locations and it can take too much time for a lab to process samples for various places. Continuing progress in miniaturization and improved output of various technologies such as computers and laser diodes allow for compact and field-portable sensors to be realized and used for quick on-site analysis and decision making.

One of the largest industries in Alberta revolves around mining oil sands and extracting crude oil from them. This process results in large amounts of oil sand tailings which are collected and stored in large ponds. Tailing are sands and clays mixed with water which also contain some small amount of bitumen unable to be extracted and is hazardous to wildlife. The tailings are liquid in nature and are collected in ponds so that they can settle and water can be recycled. It takes about 10 parts water to produce 1 part of bitumen and roughly 65% of the water can be recovered from the initial settling of the tailings after a couple years. [1] Unfortunately, the remaining tailings known as Mature Fine Tailings (MFT) can take decades or more to finish settling [1], [2] but once the tailings are consolidated and are more solid in nature, they can be more easily transported and sequestered. The water reclaimed from the solids can be recycled to be reused which is valuable because continual input of water can be environmentally expensive and the volume of water trapped in tailings take up the majority of space in ever-increasing tailings ponds. Thus a major challenge is to manage the oil sands tailings in temporary holding ponds, processing it, and finally reclaiming the ponds. One of the overall challenges of the tailings is that its makeup is very inconsistent. Some general properties are defined for it, but the specifics depends upon things such as the exact mine site and particulars about each company's extraction methods. A number of ways are being investigated and implemented to speed up the consolidation process or otherwise deal

with the tailings: filtering, evaporation or drying, centrifuging, freeze/thaw, vegetation transpiration, chemical or biological flocculation and coagulation, mixing with various soils and permanent storage are some of the general methods. [1] Centrifuges can increase settling rates by applying thousands of times of the force of gravity to the tailings and directly increasing the settling rate of the particles. Flocculants typically alter the interaction chemistry between particles by either grouping them together (larger particles tend to settle faster) and by changing the electrostatic properties of the solution. The small particles or fines can be suspended due to electrostatic forces which balance the gravitational forces for settling and changing the pH can alter these interactions.

One key property of interest is the 'solids content' (s.c.) of the tailings, which is its weight per weight concentration which describes how solid or settled it is. The traditional way to measure this is to compare the weight of a sample before and after oven drying it, which is time consuming. It requires human intervention to deal with each step in the measurement and analysis process which is doubly inconvenient when in a remote location. Other methods which can be used include gamma ray measurement, neutron scattering, and frequency or time domain techniques which may require sample preparation, be offline, or have social stigmas from 'nuclear technology'. [2] Light scatter is yet another method which was chosen as the method to study. It has advantages of being safe, as we are exposed to visible light all the time; clean, as there are no by-products from measurement; and non-contact, as the sample does not need to be disturbed or destroyed in any way. By design it can also be widely available and does not require exotic sources, it does not need to consume large amounts of power, and after installation it can be fully automated and transmit its data via the internet which can be made available in even the most remote of locations.

An inexpensive, compact sensor will help the evaluation of the various techniques and allow for as many variations of trials to be tested in parallel as desired with the impact on instrumentation cost and personnel required minimized. A quick and in-situ sensor allows rapid decision making and allows the sensor to even be applied to flowing pipelines for process optimisation. Fluorescence spectroscopy is used here for sample composition analysis. Cone penetration is a technique for measuring physical properties of subsurface soils and can be equipped to carry out other measurements. Laser diodes enable the light source for the sensors to be compact, cost effective and have high power output with their widespread use and availability in consumer electronics. Light scatter techniques is used here for solid content analysis. The following sections will discuss these technologies in further detail and how they contribute to the development of the sensors.

## **1.1 Fluorescence:**

Fluorescence is a standard technique to determine the chemical components of a sample. Simply put, it is the light emitted from a compound which is excited; typically, from another light source with shorter wavelength. The light emitted is analyzed by a spectrometer which was once immobile, but today they continue to be miniaturized, and while the trade-off is usually resolution and sensitivity, the performance is still more than sufficient for many field testing purposes. If the signature fluorescence spectrum of a compound is known, this technique can be used to identify contaminants at a location and if none can be found the sample can then be sent off for further analysis. Fluorescence is commonly used for contamination detection and here it is important for making sure that hazardous chemicals are contained properly and that any recycled materials or water have been sufficiently purified when they are returned to the environment.

Portable fluorescence instrumentation have been developed for some time [3] and specifically, a portable water sensor has been developed by this research group with multiple excitation wavelengths to detect Naphthenic Acids (NAs) in water affected by industrial processes. [4] Naphthenic acids are hydrocarbons from refining crude oil which are both toxic to aquatic wildlife [5] and corrosive to industrial equipment. [6]

## **1.2 Spectrometer:**

A spectrometer is a device which measures the spectral intensity of the input light and can have sub-nanometer wavelength resolution. The input light is spatially separated into its constituent frequencies and is then measured by a detector such as a linear CCD. Commercial spectrometers typically use a grating to disperse the light, but this can be difficult to align in a very compact system. Another approach is to use filters to differentiate frequencies of light. This can greatly simplify the optics of the spectrometer; however, it is at the cost of resolution.

## **1.3 Cone Penetration:**

Cone penetration (CPT) is a technique where a narrow probe is hydraulically pushed tens of metres into the ground to gather data about physical properties of the soil and determine what soil types lay beneath. The probe can also be equipped to detect chemical presence and currently UV LEDs are used with photodiodes to detect the presence of fluorescence. [7] In order to fit into the cone penetration probe, the sensor will be designed to have a maximum 25.4 mm or 1 inch diameter. The water sensor previously developed by the group can be miniaturized to fit into this 25.4 mm

diameter and applied to soil sensing of fluorescing contaminants. Having spectral resolution of the fluorescence could give knowledge of exactly what the substance is and if it is natural or a contaminant.

## **1.4 Chemicals of Interest**

The chemicals targeted by the fluorescence sensor which motivate this project include naphthenic acids, crude oil and mature fine tailings (MFT). Naphthenic acids are a common contaminant in water used for oil-related industrial processes and are highly toxic to aquatic life as well highly corrosive to equipment. [3] They are a class of compounds and their general characteristics include a combination of hydrocarbon rings and the eponymous acid group.

MFTs are by-products of certain mining and extraction processes and tend to contain bitumen or crude oil. These fluids, including gasoline and diesel which are some of their refined products, also contain multi-ringed hydrocarbons also known as aromatics. These are some of the possible targets for soil contamination testing with a fluorescence sensor in an oil-related industrial environment. Naphthalene, phenanthrene and pyrene are 2-, 3-, and 4-ring hydrocarbons which are used in testing the fluorescence sensor because they are constituents of those fluids.

## **1.5 Laser Diodes:**

Laser diode technology has advanced to a point where it is mass produced such as in movie theatre projectors or for consumer electronics in DVD and Blu-ray devices or somewhat dangerous laser pointers. They are available in relatively high power, widely available, and are extremely inexpensive as is evidenced by the number of people on the internet who make videos of popping balloons and burning household objects with laser diodes. Taking advantage of the existing supply would help to give the advantage of developing an economical sensor. The 405 nm wavelength (Blu-ray) laser diode is of sufficient photon energy to stimulate fluorescence in the hydrocarbons tested, but the 405 nm wavelength is not expected to be as efficient as UV wavelengths, which will be discussed in Section 2.1. This is offset in part by its availability at much higher power output (~100 mW) compared to typical UV LED sources (~1 mW). The other motivation for choosing this laser diode is its cost and compact form factor. The laser diodes used here have a 5.6 mm diameter body compared to commonly used excitation light sources such as gas lamps, which are typically much larger and may also require a monochromator and other optics which consume more space. This is the choice for the excitation source for fluorescence.

For light scatter measurements, both red and blue laser diodes will be used because the wavelength to particle size ratio affects the amount of light scatter. Red laser diodes have been around for longer and a variety of wavelengths beyond 600 nm are available for use.

## **1.6 Light Scatter:**

Light scatter is currently used commercially to measure particle size and concentration of dilute and prepared samples. [8], [9] Ideally, this should be applied to the denser (>30% w/w), mud-like samples without preparation in-situ which are found in oilsands tailings. Due to the concentration of these samples they are opaque and backscattering is used. This also simplifies the device as both the laser and detector are physically together and no additional paraphernalia or alignment is required like in transmissive or absorptive measurements, but the laser and detector must be arranged to avoid the specular reflection. In a general sense, light scatter is the light reflected from a particle or surface at 'unusual' angles because of its microscopic shape as compared to a flat surface. It is further complicated by internal reflections and transmissions inside the particle and the interference of these rays at the detector. Macroscopically, one can imagine that more particles will generally scatter more light, and this is the basis of how the solids content (or concentration) can be measured.

## **1.7 Description of Project:**

This project was focussed on developing light based sensors to measure an array of properties in and out of various industrial processes. On one hand is fluorescence based detection for contamination and chemical identification. On the other hand is light scatter to characterise slurry density, concentration or particle size. Light based sensors are advantageous because of their ability to be non-contact, non-destructive, economical, real-time, safe in this implementation, and software automated without moving parts. Two main devices were developed: for compact and portable fluorescence measurement, and for slurry solids density applied to 3 different scenarios.

The following chapter looks at the basic theory for fluorescence and for the known case of light scatter for a single sphere. Chapter 3 focusses on utilising fluorescence as a method of detecting hydrocarbon contamination in soils. The development and results of the fluorescence spectrometer constructed is shown. Chapter 4 focusses on light scatter as a method of characterising slurry-type samples. The light scatter sensor is applied to three different measurement scenarios and the results

of each field test in those scenarios. Chapter 5 gives a summary of the devices developed and directions to be pursued in the future.

## 2. Theory:

### 2.1 Fluorescence:

Fluorescence is the emission of photons or light wave from an excited atom or molecule. If it occurs quickly (less than  $10^{-7}$  s) it is termed fluorescence instead of phosphorescence. This difference is due to the lifetimes of the singlet and triplet states respectively. When a photon is absorbed, some of the photons can be emitted at a slightly different energy, known as a Stokes transition, with the difference accounted for in final energy state of the molecule. These emitted photons of shifted wavelength are characteristic to the material and can be used as a fingerprint for identification. [10] A general property of fluorescence is that the fluorescence spectrum is independent of the excitation wavelength and this is known as Kasha's rule. Additionally, the quantum yield, or efficiency of photons absorbed to photons emitted is also constant. [11] This is due to higher excitation states undergoing vibrational relaxation (non-radiative) to the lowest vibrational excited state which occurs in a faster timescale compared to radiative transition. Once it has quickly reached the lowest vibrational excited state, it then relaxes radiatively in the signature spectra. However, this is not necessarily true for complex molecules and especially aromatic compounds which can have different relaxation pathways. [12] It has been seen [13], [14] that the fluorescence emission peak shifts to lower wavelengths as the excitation wavelength is decreased for petroleum contaminants which contain the compounds tested here. It is also noted that the fluorescence intensity also increases (to a point) as the excitation photon energy increases. For example, gas condensate, gasoline, flare pit residue and heavy crude oil which all are composed of various aromatic compounds including the ones tested here were reported [13] to have peak fluorescence intensity in UV wavelengths below 405 nm. It is expected that the same pattern holds for the pure compounds separately. According to this information, 405 nm is not the optimal choice for excitation, but it is sufficient to stimulate fluorescence and its availability at high output power ( $\sim 100$  mW) compared to UV LEDs or lamps sources ( $\approx < 1$  mW) is used to compensate for the lower fluorescence intensity.

The variation in fluorescence emission spectrum with excitation wavelength can be used to obtain an even more unique fingerprint of a material known as an excitation-emission matrix (EEM). An EEM is a 3-dimensional plot where the fluorescence intensity is plotted against both the emission wavelengths and excitation wavelengths. Different excitation wavelengths can cause different fluorescence spectra and even if two substances have similar fluorescence at one excitation

wavelength, it is likely that they will be different at others. Further analysis can be done on an EEM to determine specific compounds present in a mixture such as crude oil or diesel. [13] In this study, the three pure compounds tested – naphthalene, phenanthrene, and pyrene – are constituents of gasoline, crude oil and other contaminants to be detected.

## 2.2 Light Scatter:

When light passes by an atom which has no resonances (e.g. vibrational, electronic) at that energy, the electric field causes the electron clouds around to oscillate. The light elastically scattered when the oscillation immediately causes the re-emission with the same energy in a random direction. [10] In a perfect, homogenous medium, for each atom

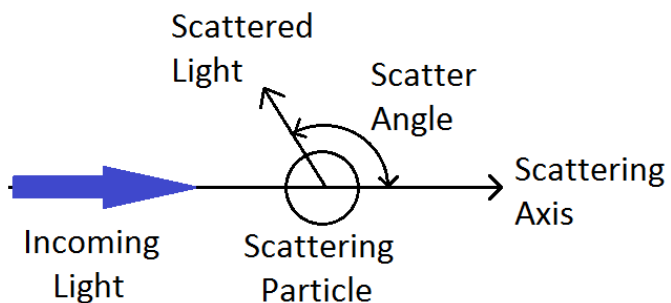
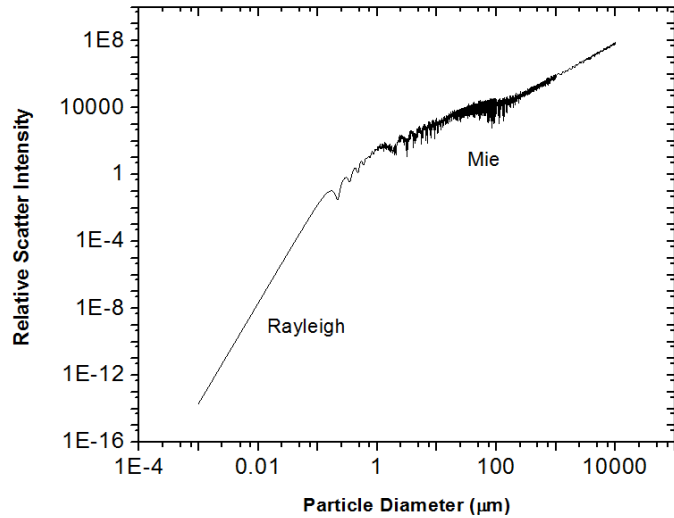


Figure 2-1 – Schematic of light scattering geometry. The scattering angle is measured with respect to the direction of unimpeded light.

which scatters, another can be found which is located half a wavelength away which causes destructive interference and negates scatter. Inhomogeneities such as molecule orientation in liquids and gases or particles suspended in other media disrupt this interference and are the source of scattered light. [10], [15] For the discussion of scattered light in this thesis, the scattering angle is measured as the angle between the vectors of incoming light and scattered light as shown in Figure 2-1. The angles of interest in this work are typically greater than  $90^\circ$ , which is also known as the backscatter. Often the backscatter angle will be used; this is the supplement to the angle of scatter, or  $180^\circ$  minus the scatter angle shown.

Light scatter exists in three different regimes: Rayleigh, Mie and diffraction or geometric optics. [2], [15] Rayleigh scattering occurs, as in the sky, when the particle diameter is much smaller than the wavelength of the incident light, and the particle can be considered to be in a uniform electric field. The well-known result of this is that the scattering intensity is proportional to  $\lambda^{-4}$ . At the limit of a very large particle compared to the wavelength of the light, the particle is large enough that rays can be considered to reflect and refract off the particle/medium boundary. The total scattering arises from the interference of these rays as well as the diffraction of the particle. Finally, the range where the particle size and wavelength of light are similar requires Mie theory, which is a formal solution to Maxwell's equations for scattering from a sphere of arbitrary size. The end result can be used to

numerically calculate scatter coefficients given particle size, observation angle, wavelength and index of refraction of the particle and medium. Then the amount of light scatter can be calculated and plotted. With the rise of personal computing power, software for calculating light scatter is available for a variety of platforms including Matlab, Fortran, Python and C based upon a text by Bohren and Huffman [16]. For this project, the one primarily used, 'MiePlot', is a packaged Windows



**Figure 2-2 – Scatter intensity calculated with MiePlot program for a single scatterer at 160° and 405 nm wavelength. The scatter intensity increases in general with particle diameter. Rayleigh particle size region is labeled and Mie region shows more**

software which has a helpful user interface and is set up to run a wide variety of situations such as scatter intensity vs. scattering angle, diameter, wavelength, and index of refraction, as well as a large amount of other situations. [17] Another capability it has is the Debye solution for Mie scattering. The Debye solution yields the same results, but envisions that light rays incident on the particle reflect and refract multiple times internally and is summed up in total to give the scatter pattern. Each mode is calculated and can be displayed separately to give some insight to what contributes to the complex scatter patterns.

The wavelength range considered in this project is visible light: 400 to 700 nm and the particle sizes common in slurries are around 500 nm to a few millimetres. Therefore the light scatter is calculated by Mie theory which is valid for any particle size although it is much less computationally efficient compared to special case limits such as Rayleigh scattering.

The MiePlot program calculates only for a single spherical scatterer. This was used to gain a general understanding of the light scatter response with respect to particle size. Simulations, such as the one shown in Figure 2-2, were primarily done at a scattering angle of 160° (or 20° backscatter) to match with the choice of angle in the devices made. In general, increase in particle size increased the amount of scatter with finer details in the Mie scatter region.

One major difference in the available theory and the cases being tested is the particle concentration. In much of the literature and commercial devices, samples are diluted to achieve the 'single scatterer' condition. In the literature found, samples which are considered highly concentrated well past the single scatterer limit, but are still dilute enough to analyse using a transmissive technique; they are usually <5% w/w concentration compared with >30% w/w being measured here.

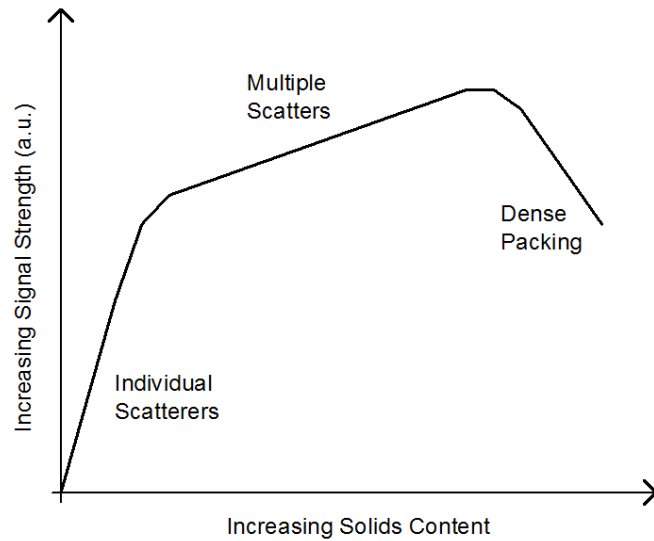


**Figure 2-3 – Plot showing the scatter intensity in relation to the solids content. Three regions occur for dilute, concentrated and highly concentrated particles.**

When testing with polystyrene beads and sand/clay mixtures, 3 main regions were found. Different mixtures of different types (shapes) of sand, silt, clay, or beads are expected to differ from one another, but in general: when dilute, typically from 0% to 10% w/w, the light scatter increased rapidly with concentration. The mid-range, 10% to around 70% w/w, increased much more slowly, in comparison. Beyond 70% w/w, the signal starts to decrease again. The dry sample, which is naively 100%, has a much higher signal which was measured as 3 times larger than the mid-range scatter. The reason for this is explained below.

This behaviour was interpreted as follows: In the dilute region, each particle is a single scatterer and the amount of light scattered increases in direct proportion to the number of particles. In the middle region, the particles are beginning to screen one another from the incident laser light, thus the amount of light scattered will not increase by the same magnitude for each additional particle. Multiple scattering also becomes common which increases the amount of light scattered to the sides as opposed to the front or back. At the very highly concentrated region, the signal begins to decrease. One possible explanation for this is that there is very tight packing of the particles. A factor which contributes to light scatter is the contrast of the refractive index of the particle and the medium. If the particles are packed so tightly they touch one another, light does not have an interface to reflect or scatter off of, and continues travelling until it is absorbed. In the limit where the particles could be packed to 100%, they would simply be a solid block and the light scatter

would be very low, depending on the roughness of the surface. The dry sample should not be considered 100%, because it has air voids between the particles; it is a loose powder or a porous material. Since scatter depends on the index of refraction ratio of the particle to the medium, air ( $\approx 1$ ) compared to water ( $\approx 1.33$ ) at visible wavelengths would have a higher ratio and be expected to scatter more light.

### 2.3 Settling:

In the simple case of non-interacting particles in a fluid, a particle experiences 3 forces: gravity, buoyancy, and drag as it settles. Force due to gravity is:

$$F_g = \rho_p \cdot \frac{\pi}{6} d^3 \cdot g \quad (1)$$

Where  $\rho_p$  is the density and  $d$  is the diameter of a particle, and  $g$  is acceleration of Earth's gravity. If inside a centrifuge,  $g$  can be replaced by  $r \cdot \omega^2$ , the radius of the centrifuge arm and the angular velocity respectively.

The force from buoyancy is due to the weight of the fluid displaced by the particle:

$$F_b = \rho_w \cdot \frac{\pi}{6} d^3 \cdot g \quad (2)$$

Where  $\rho_w$  is the density of water, which is the typical fluid here,  $d$  is the particle diameter and  $g$  is the acceleration due to gravity.

The drag force is given by Stokes' Law because the Reynolds number is expected to be small due to the small size and slow speed of the particle in water.

$$F_d = 3\pi \cdot \mu \cdot d \cdot v_p \quad (3)$$

Where  $\mu$  is the viscosity of water,  $d$  is a particle diameter, and  $v_p$  is the settling velocity of the particle. Using these three forces in equations 1-3, the net force can be calculated as:

$$F_{Settle} = m_p \cdot \frac{dv_p}{dt} = F_g - F_b - F_d = (\rho_p - \rho_w) \cdot \frac{\pi}{6} d^3 \cdot g - 3\pi \cdot \mu \cdot d \cdot v_p \quad (4)$$

Where the positive direction is downwards. Solving this differential equation in the typical way with an integrating factor will give the time-dependent settling velocity of the particle:

$$v_p(t) = \frac{g \cdot \Delta\rho \cdot d^2}{18\mu} (1 - e^{-at}) \quad (5)$$

Where  $g$  is the gravitational acceleration,  $\Delta\rho$  is the difference in density between the particle and water,  $d$  is the particle diameter, and  $\mu$  is the viscosity of water. The exponential  $\alpha$  is a collection of constants from integration, depends on the viscosity of the fluid, and size of the particle. For the value ranges of interest,  $\alpha t$  is expected to be large and thus  $e^{-\alpha t} \approx 0$ . This implies that the terminal velocity for the particle is reached quickly and approximates settling at a constant velocity. What this analysis does not consider is the particle interactions which undoubtedly occur due to the high concentrations. However, the settling velocity of a particle is proportional to the square of the diameter which gives a good general picture of how the slurry settles. Another thing to consider is the electrostatic forces, depending on the structure of the particle material, which can result in 0 net force for sufficiently small particles. [1] Additives can be added to alter the pH chemistry of the slurry to negate the electrostatic forces in an effort let the smaller particles settle.

### **3. Fluorescence Spectrometer**

The first device developed in this work was a fluorescence spectrometer in collaboration with ConeTec, a company which sell site investigation equipment and services. The focus of this device is to use fluorescence as a method to detect hydrocarbon contamination in soil, but in a device which is portable and for samples which do not need to be prepared. Fluorescence spectrometers are commonly used in industry and scientific applications; however, the device here was designed to be compatible with Cone Penetration (CPT). As discussed in Section 1.3, the CPT tube requires the entire spectrometer assembly to be able to fit into a 25.4 mm diameter tube. Work was previously done in the research group to develop and build a fluorescence-based sensor for water contamination testing and this spectrometer builds upon that work.

#### **3.1 Previous Work**

Previously in this group, a portable spectroscopic bench-top sensor was developed for testing contamination levels of process-affected water. This sensor used multiple excitation wavelengths to create an EEM using 6 LEDs with UV wavelengths ranging from 265 to 340 nm. The sensor was a tall cylinder (12 cm x 53 cm) and weighed 4 kg. This device was highly successful in detecting low concentrations of hydrocarbon contamination in unprepared process affected water samples. [4]

The next step was to create a CPT compatible spectrometer. The sensor used in the bench-top model was an Ocean Optics USB spectrometer which is too large (9 cm x 6 cm x 3 cm) for this design and commercial spectrometers small enough for this design are not yet widely available. Given the 25.4 mm diameter limitation, a design using a prism in conjunction with a linear CCD detector was developed to create a high resolution spectrometer. It was difficult to achieve good alignment, but a resolution of 15 nm to 18 nm was achieved with a collimated white light source. [3] Therefore, an approach was taken to create a lower resolution spectrometer but with much more simplified optics and alignment. This design will trade resolution, simplifying the optics used to obtain spectral information of the fluorescence, by using long-pass filters to create a robust and cost-effective sensor.

### 3.2 Design

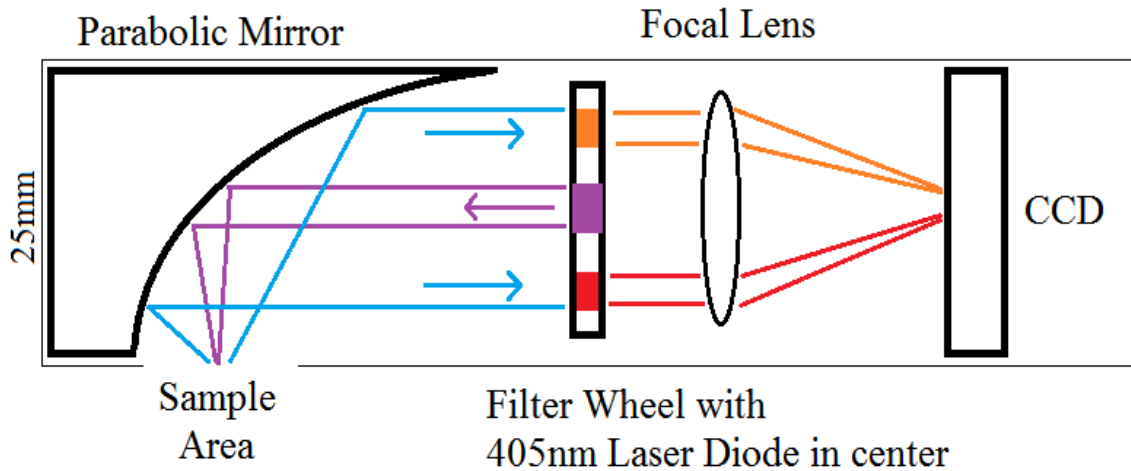


Figure 3-1 – Schematic of setup. Excitation source in center of ‘filter wheel’ is focussed by the parabolic mirror onto sample area. Fluoresced light is collected by the parabolic mirror, passes through filters and is focussed onto imaging CCD. [3]

The excitation source uses a 150 mW laser diode with a wavelength of 405 nm (blue/violet). As discussed previously (Section 2.1) the excitation wavelength would ideally be UV, but it is sufficient for stimulating fluorescence and its high output power, compact form factor (5.6 mm diameter) and low cost make it a better candidate for this sensor compared to UV LEDs or lamp sources. Other typical laser diode wavelengths of 532 nm (green) and 650 nm (red) are not used because they have even lower photon energy and are expected to have lower fluorescence efficiency while they have similar output power and cost compared to the blue/violet laser diode.

A 90° parabolic mirror is used to focus the excitation light at a right angle on the sample, to collect the fluoresced light and to collimate it. Reusing focussing optics reduces the footprint and it can simplify alignment. The collimated, fluoresced light is then passed through the ‘filter wheel’. The filter wheel pictured in the lower right of Figure 3-2 is a 25 mm diameter aluminium frame holding a set of 5 coloured glass filters

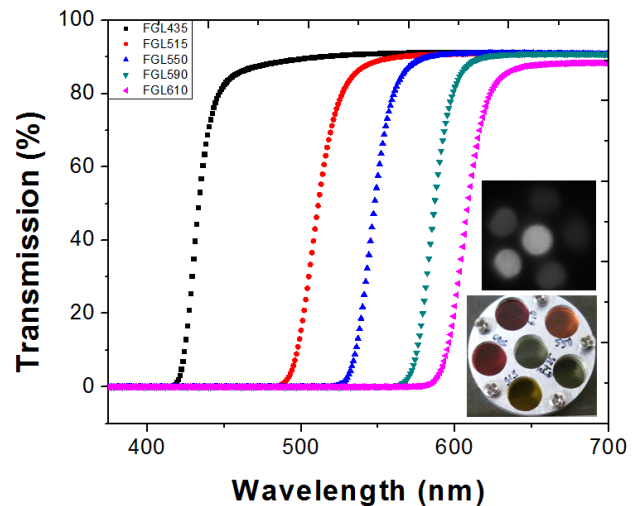


Figure 3-2 – Transmission spectra of 5 filters used. Lower right: image of the filter wheel; middle location will hold excitation laser diode. Upper right: sample image captured from device. Colour available in electronic version.

arranged around the outer edge. The filters used are long-pass filters, which mean they transmit light with a wavelength longer than its cut-off wavelength. The filters were cut by water jet to a diameter of 7 mm. The center of the filter wheel is reserved for the excitation laser diode. The 5 filters have successive cut-off wavelengths: 435 nm, 515 nm, 550 nm, 590 nm and 610 nm.

A 1 inch, f/2, biconvex, spherical lens is used to focus the filtered light onto a CCD detector to be analyzed. The intensity of the fluorescence depends on the intensity of the excitation light and the concentration of analyte. Focussing the fluorescence improves the sensitivity of the sensor by increasing the intensity of fluoresce because the same number of photons are concentrated into a smaller area. This allows for a larger signal for a given excitation power and analyte concentration. Focussing the collected fluorescent light into a smaller area also decreases the footprint of the CCD required and helps to achieve the 25 mm diameter specification. The CCD used is a PointGrey Chameleon which is a silicon, monochromatic, USB camera with 1296 x 964 pixel resolution and 6.26 x 5.01 mm imaging area using a 12 bit analog to digital converter [18].

### 3.3 Analysis method

The CCD used is monochromatic therefore the outputs of the filters are determined spatially on the image captured. The output is a greyscale image depicting the intensity of light transmitted by each filter shown in the upper right inset of Figure 3-3. The value reported in the image corresponds to the signal due to light of all wavelengths longer than that of the cut-off wavelength of the filter. The difference between the signals of two different filters will reveal the amount of fluorescence in the wavelength band between the cut-offs. The excitation light has a wavelength of 405 nm and is filtered out by all of the filters. The transmission spectra of the filters were measured with a Perkin-Elmer NIR-UV Spectrometer and displayed in Figure 3-2. For example, the '435 nm' and '515 nm' filters transmit light with wavelengths larger than 435 nm or 515 nm respectively. Therefore the

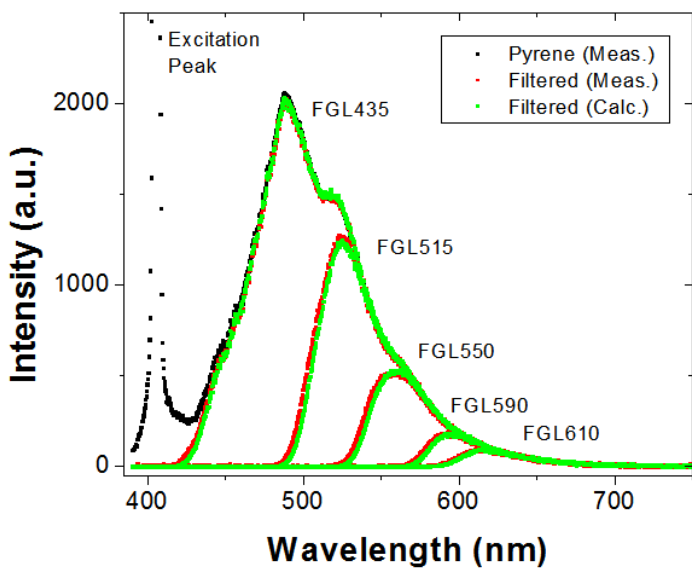


Figure 3-3 – Pyrene fluorescence spectra. Laser diode excitation peak (405nm) and effects of each filter shown. Measured and calculated spectra (red, green) are well matched. Colour available in electronic version.

difference in signal between the two filters corresponds to the amount of fluorescence in the wavelength range of 435 nm to 515 nm. By doing this with pairs of filters, the spectrum can be reconstructed in sections. Consequently, using more filters results in higher resolution.

The pairs of long-pass filters work similarly to band-pass filters since it is being used to measure the light intensity in a short spectrum segment. It has the disadvantage of taking up twice the space (two filters) needed to simulate a band-pass filter but this is offset by the fact that long-pass filters are more available in the desired increments along the visible spectrum compared to band-pass filters. These coloured glass filters have a relatively sharp transition and constant transmission spectrum compared to their band-pass counterparts. Dielectric band-pass filters can have excellent transition, transmission and cut-off characteristics and they can be designed for any wavelength range desired using appropriate materials, but they have an increased cost.

The image captured is analysed in ImageJ, a Java image processing freeware. An average pixel intensity of the monochromatic image is taken at each of the 'filter spots' which is spatially associated to each filter. These numbers are entered into an Excel spreadsheet template developed to quickly analyze the image. In this setup, the excitation laser diode is placed externally and focused on the sample instead of being mounted in the filter wheel. This is done to provide easy access to both the laser diode and internal components of the setup during prototyping. In place of the laser diode, a second 435 nm cut-off filter was placed in the center slot as a placeholder. The value measured from the image is the intensity of the light on a pixel, modified by the spectral sensitivity of the CCD. Therefore the intensity of each spectral band of the fluorescence is calculated by subtracting the signals from adjacent filters. Thus there are 4 wavelength bands: 435 nm – 515 nm, 515 nm – 550 nm, 550 nm – 590 nm, and 590 nm – 610 nm. These values are then normalized for comparison with a high resolution spectrum.

For comparison, a high resolution spectrum is measured using an OceanOptics USB2000 spectrometer. The signal is then modified according to the CCD wavelength sensitivity and for each filter transmission spectrum. In Figure 3-3 the effect of each filter is shown on a typical fluorescence spectrum (Pyrene shown here). The cut-off wavelength in nanometres is given by the number in the filters' model number. These 5 signals are then integrated which equates them to the data collected from the CCD image, and analyzed in the same way by subtracting adjacent filter intensities.

### 3.4 Results

Initial testing and results were obtained from red and green fluorescent paper due to their high fluorescence efficiency and thus high intensity fluorescence. The high resolution spectral response of the orange fluorescent paper shows that it peaks around 602 nm and has a full width, half maximum (FWHM) of 40 nm. The green fluorescent paper peaks around 513 nm with a FWHM of 47 nm. With the orange paper, the 590 – 610 nm range dominates in intensity and likewise with the green paper the 515 – 550 nm range has the greatest intensity. This shows a proof of concept of the device which is capable of distinguishing between the two spectral peaks 89 nm apart. The uncertainty in the measurements comes from the variation in signal when a captured image is analysed. The majority of this uncertainty comes from the tilt correction which will be discussed later.

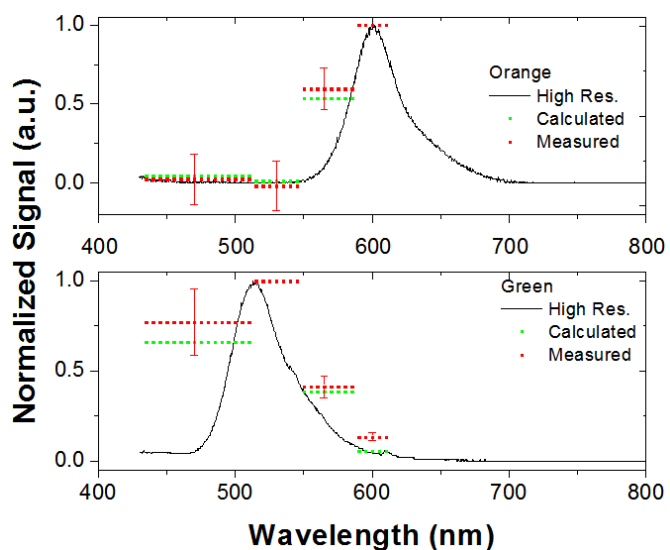


Figure 3-4 – Top: Orange fluorescent paper; Bottom: Green fluorescent paper. Colour available in electronic version.

range has the greatest intensity. This shows a proof of concept of the device which is capable of distinguishing between the two spectral peaks 89 nm apart. The uncertainty in the measurements comes from the variation in signal when a captured image is analysed. The majority of this uncertainty comes from the tilt correction which will be discussed later.

Polycyclic aromatic hydrocarbons were also used for testing to easily simulate targets of interest such as crude oil or naphthenic acids which are both composed of an unspecified mixture of such compounds. The hydrocarbons used were 2-, 3-, and 4-ringed aromatic compounds known as naphthalene, phenanthrene and pyrene, respectively. They were obtained as solid reagents and were dissolved in chloroform as chloroform was a sufficiently strong solvent and measured to have no fluorescence in the wavelength range of interest. For all three substances, this resulted in a clear, colourless solution. Unfortunately it was not possible to obtain a clear image using these samples because the solution fluoresced along the entire path of the laser beam. The parabolic mirror is focused at the cuvette-sample interface but since the sample is clear, light is collected from the focal point as well as all the points out of focus behind it resulting in a blurry and unusable image. Therefore this step was skipped and each solution was mixed with clay powder, then the chloroform was allowed to evaporate in ambient conditions. This resulted in an opaque powder of contaminated clay, which was then used as the sample. This contaminated clay sample is meant to

represent contaminated soil that would be encountered by the device in normal operation. The concentrations by weight of naphthalene, phenanthrene and pyrene are  $21 \times 10^{-3}$ ,  $34 \times 10^{-3}$  and  $69 \times 10^{-3}$  respectively.

The excitation laser (405 nm, 1.4 nm bandwidth) was used at a constant current of 50 mA (15 mW) and controlled by Team Wavelength FL593 USB controlled laser driver. Of the three hydrocarbons, pyrene has the highest fluorescence efficiency based on required integration time for similar signal strength. Its peak fluorescence occurs at 485 nm and it is visually distinguished from the excitation laser peak as seen in Figure 3-3. For

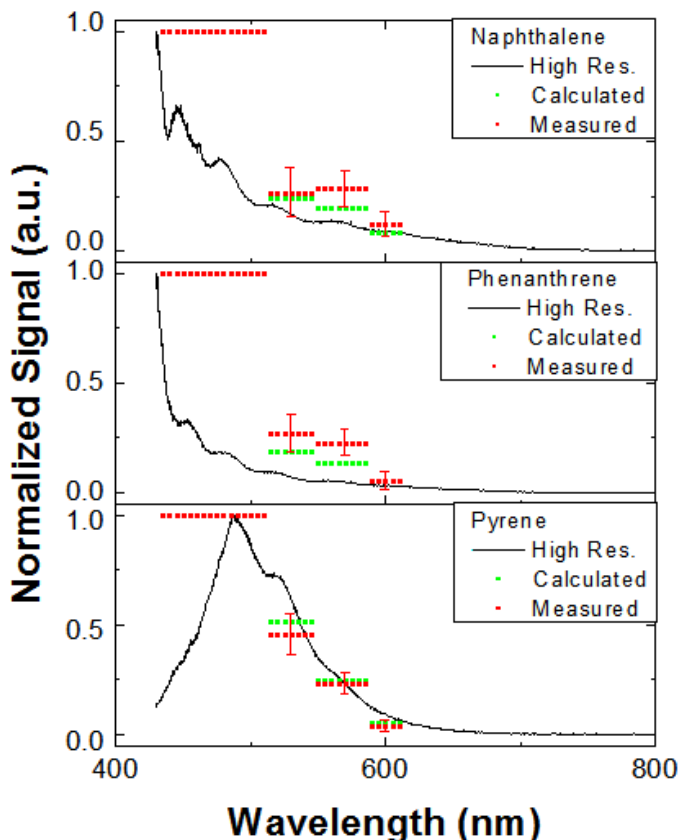


Figure 3-5 – Polycyclic hydrocarbons in clay. Concentration of 21, 34 and 69 parts per thousand for naphthalene, phenanthrene and pyrene respectively. Colour available in electronic version.

naphthalene and phenanthrene the fluorescence intensity is relatively much weaker and is so close to the laser peak that they cannot be visually distinguished. The first filter, FGL435, has its cut-off wavelength at 435 nm and its transmission below that is  $\sim 10^{-4}$ , which is sufficient for light of wavelengths shorter than the cut-off to be negligible when carrying out the analysis. All the subsequent filters have equal or less transmission at these wavelengths as expected. As seen from Figure 3-5, naphthalene and phenanthrene have very similar fluorescence spectra and much of what distinguishes them lies inside the 435 – 515 nm wavelength range so with this device the results are generally the same. Since pyrene has a relatively redder fluorescence peak, it is distinguished by higher intensity of the 515 – 550 nm, and 550 – 590 nm regions. When comparing the output of the green fluorescence paper and pyrene the fluorescence peaks are around 513 nm and 485 nm respectively. The peaks have a FWHM of 47 nm (green paper) and 74 nm (pyrene) with a peak separation of 28 nm as measured on the high resolution spectrum. Despite this, the sensor is capable of distinguishing the two peaks. This is because the green paper peak occurs essentially on the cut-off wavelength of a filter and has a redder fluorescence compared with pyrene. This

suggests a way to design the filter cut-off points in order to maximize the effectiveness of the device.

The last two materials tested were crude oil and mature fine tailings (MFT). Crude oil is the raw bitumen product which is typically sent from the extraction site to refineries, and MFT in general is the wastewater from certain mining operations. In this case the samples came from oil sands tailings in northern Alberta. These are 'field test' samples and their makeup is more complicated than single reagent chemicals. Typically the bluer fluorescence peaks come from aromatic compounds with few rings, whereas the red contributions are from many-ringed aromatics, [13] [19] so it appears that this sample of MFT has a broader variety of hydrocarbons compared with the crude oil. The crude oil had a concentration of  $6.3 \times 10^{-3}$  diluted in chloroform and the sample was black in colour and nearly opaque which was adequate to obtain a good image. MFT is composed of sands, silts, clays and water, and is 55% solids by weight, containing  $17 \times 10^{-3}$  concentration of bitumen. The MFTs used were typically a dark brown colour and opaque.

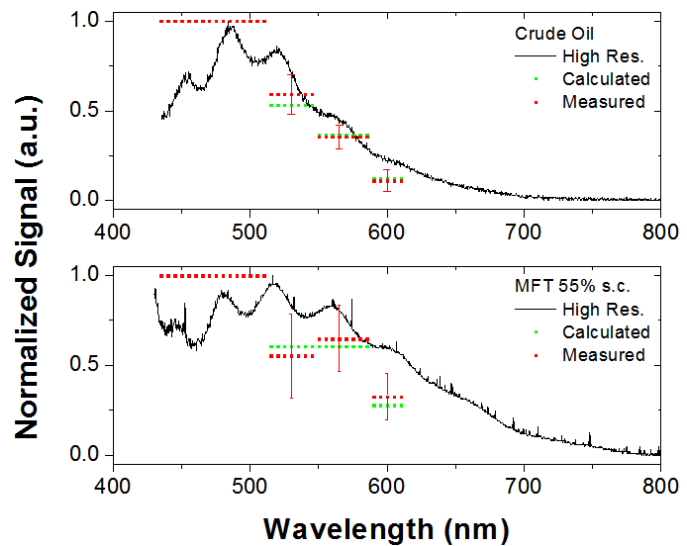


Figure 3-6 – Comparison of crude oil and MFT fluorescence with 405 nm excitation. Crude oil concentration of  $6.3 \times 10^{-3}$  and bitumen concentration in MFT  $17 \times 10^{-3}$ . Colour available in electronic version.

The high resolution fluorescence spectra, in Figure 3-6, of the two samples show that they are very similar although slightly broader for MFT. This is reflected in both the calculated and measured filter responses where the relative intensities decrease in each filter step towards the redder wavelengths for crude oil, but for MFT both the 515-550 nm and 550-590 nm bands are roughly equal in intensity.

### 3.5 Discussion

Overall this device is successful in showing a proof of concept of using incremental long-pass filters to create a simple miniaturized spectrometer. The primary drawback of it is that it has poor resolution compared to typically available spectrometers. The resolution is dominated by the

number and step size of the filters used. Currently the filters used are coloured glass, cut by water jet to a diameter of 7 mm and are spaced evenly around the 25 mm diameter frame. These filters could be cut into smaller diameters and tiled closer on the frame in squares or hexagons. Alternatively a linear variable long-pass filter or custom designed dielectric filters could be used but at much higher monetary cost.

As discussed above, previous work was done by this research group to build a high resolution sensor for CPT, but had difficulties with alignment. A goal of this design was to simplify the parts used and facilitate alignment as compared with more complex designs, such as with a prism or a grating. The setup and alignment is relatively simpler and most of the effort is applied to aligning the parabolic mirror. Since this device is still being prototyped, the components are not fixed as rigidly as would be in a final product and the alignment could change over time. The CCD was clamped into position above the setup but it would have to be moved aside for lens or filter adjustments to be made. If the CCD was tilted by a few degrees, the image would brighten or darken on the left or right side since the sensor is sensitive to the angle of incident light. The alignment of the parabolic mirror also contributed to this tilt effect and the best alignment achieved did not fix this problem. In attempt to correct this, the data was collected once with the filter in place and once with the filter removed to calculate an adjustment factor based on the distribution of brightness without the filters. This contributed much more to the uncertainty compared to measurement of the filtered images and was the primary source of error.

Another source of error contributing to the discrepancy between the measured and calculated filter values is from optical aberration. After the fluoresced light is collected and collimated by the parabolic mirror and passed through the filters, it is focussed onto the CCD using a 1 inch,  $f/2$  biconvex spherical lens. Since the setup is designed to fit into a 25 mm column and the filters are arranged around a central excitation source on the filter wheel, to utilize the full diameter an aspheric lens should be used. In the analysis the outermost edges of the image were avoided to minimize the effect of aberration.

When comparing the device results of several similar fluorescence such as naphthalene and phenanthrene or MFT and crude oil, using the 405 nm excitation wavelength yields very similar results. This is where an EEM would be useful to compare the fluorescence from different excitation wavelengths. To implement this in the device a few LEDs of different wavelengths could be fiber-coupled to reduce their footprint and be individually activated. This was designed previously for the

device [3] but was not used here in favour of the single laser diode. More filters can be used to achieve better resolution, but if this device is to be used in a cone penetration device and substances of interest are known, the resolution may not need to be as high as for general purpose spectrometers. Using a library to match known fluorescence output in combination with an EEM may be sufficient for contamination detection. The limit of detection should also be determined for this device. One challenge which may occur if this device is used in a cone penetration device is in its sampling window. Since the cone is pushed forcefully into various types of earth, the window needs to be able to withstand scratching and repel substances which may stick to its surface.

As an example of how this device would be used for real-world applications, two similar samples can be considered. In Figure 3-7, gasoline and diesel are diluted in chloroform and the fluorescence from 405 nm wavelength excitation is measured with a high resolution Ocean Optics spectrometer. The expected signals from the device are also calculated. The biggest difference between these two similar spectra lies in the 500 – 600 nm wavelength range. In

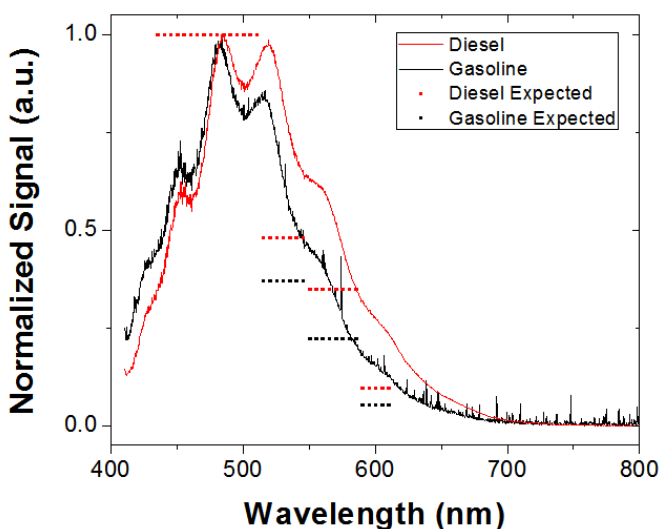


Figure 3-7 – Fluorescence signal from diesel and gasoline @405 nm excitation. Colour available in electronic version.

this range, the diesel signal is somewhat stronger compared with the gasoline. Likewise, the two calculated output from the filters (515 – 550 nm and 550 – 590 nm) reflect diesel having a stronger signal. If this device were to be designed to differentiate between gasoline and diesel, the choices of filters would be to create as many sections as possible in this range to focus the resolution here. Additionally, the signal uncertainty in the prototype would have to be improved in order to clearly differentiate between the two samples.

An additional aspect of the analysis is the absolute intensity of the fluorescence signal. The intensity of the signal is affected primarily by the quantum yield of the fluorophore and the concentration of the sample. A result of the simple design of the optics in this device is that it is relatively simple to calculate the counts per second of the fluorescence. The parabolic mirror has a 1 inch collection diameter spaced 2 inches away from the sample, and it is focussed by a simple lens onto the CCD.

The CCD has a conversion efficiency given by the manufacturer at which it converts a photon hitting a pixel into one count. The shutter time is controlled manually such that the CCD signal does not saturate and thus can be factored in. By using this information, the number of photons per second which are emitted by the sample can be calculated.

In summary, the following things are used to calculate the fluorescence of the sample. The quantum efficiency of the CCD as given by the manufacturer is used, which gives the CCD's conversion from photons to signal counts. The manufacturer's data is spectrally resolved and a weighted average is taken based on the high resolution spectrum of the sample. The reflected loss from the optics (i.e., CCD, focussing lens, filters, and cuvette) is approximated as a 4% loss per surface. The average pass-band transmission of the filter is measured to be approximately 90% and the average reflectivity of the aluminum parabolic mirror is also 90% in this wavelength range according to the manufacturer. The parabolic mirror has a collection angle  $2\theta = 28^\circ$  and assuming isotropic spherical emission of the fluorescence, the fraction of the solid angle collected is 0.015. The intensity measured is the average of a single pixel, (a  $3.75 \mu\text{m}$  square) and the total area of the image is approximately an 8.5 mm diameter circle. The excitation laser diode output power was calibrated and under typical operating conditions (50 mA drive current) the total power is 4 mW.

Using this approach, the fluorescence efficiency of each measured sample is calculated. Since the range of this spectrometer begins at 435 nm, only fluorescence from 435 nm to approximately 800 nm is measured. The 800 nm cut-off is due to sensitivity limitations of the CCD camera used. The

<b>Sample</b>	<b>Efficiency</b>
Naphthalene	0.21%
Phenanthrene	0.13%
Pyrene	1.91%
Green Fluorescent Paper	11%
Orange Fluorescent Paper	15%

results are summarized in Table 3-1. Two pieces of fluorescent paper, orange and green, are shown as well as the three polycyclic hydrocarbon compounds. The typical choice for fluorescence studies of these compounds are UV source excitations so it is difficult to compare these results directly. For example, when excited with 265 nm wavelength light, naphthalene was measured to

have a 23% quantum yield diluted in cyclohexane [19] which is orders of magnitude greater than what was measured with 405 nm. Similarly, phenanthrene and pyrene have quantum yields of 13% and 32% when excited at 254 nm and 313 nm respectively. The samples measured here are dry, diluted and prepared as described above; this, as well as concentration may have effect on the

fluorescence efficiency found here. Although the efficiency is lower, for the purpose of the device, the magnitude of fluorescence signal is still high because the 405 nm laser diode is capable of high output power and is simpler to collimate and focus compared with a UV LED, especially with these space constraints.

### **3.6 Field Test Design:**

Currently, this spectrometer is in an early prototyping stage; the current setup was built to facilitate testing in the lab environment and some changes will have to be made to realize a model for field testing.

The current parabolic mirror is 90° off-axis used has a reflected focal length of 2" which allows for working room between the sample holder and the setup. In the design, the focal point of the mirror should be on the surface of the window because the 'sample' will be surrounding the instrument and pressed up against the window. Therefore it would be necessary to change the mirror either to one of shorter focal length (1/2") or use one with a different off-axis angle. For example, a 30° off-axis parabolic mirror with 27.22 mm reflected focal length gives a focal point 13.6 mm radially from the center of the tube which has an inner diameter of 25.4 mm or 1". This makes the focal point on the surface of the tube and close to ideal for this design.

The excitation laser diode will be mounted inside the instrument, in the reserved location at the center of the filter wheel. As mentioned above, the laser diode was positioned externally in this lab setup for ease of access. The reserved slot is 7 mm in diameter which will fit a small housing for the TO-56 laser diode (5.6 mm diameter package) along with the 5 mm diameter collimating lens.

The current CCD camera used is a commercial plug and play USB camera which is available and commonly used in this lab. It is a camera intended for scientific use; therefore it has a full array of technical documentation which allows control over every aspect of its function. While the CCD itself is a standard 1/3" CCD (16.0 x 14 mm), including its plastic housing and electronics board it is too large for tube. Images are also currently captured manually on a laptop but this could be automated with programming from LABView.

Inexpensive cameras are available using the same or similar 1/3" CCD or CMOS sensors with a similar resolution of around 1200x900 pixels but packaged with >25mm diameter. They can be as

small as 9mm x 9mm which is due in part to a small fad in hidden spy cameras and related media. Such cameras are also commonly used in hobbyist projects which can become quite elaborate and technical. This indicates that there is availability of documentation to properly control and develop programming to acquire the necessary images. If the CCD sensor used is known (it is typically listed), the manufacturer, e.g., Sony, Casio, Cannon, will have specifications such as spectral sensitivity available. The CCD is also not required to operate with high frame rate. The typical speed for cone penetration is 1-2 cm/s. [7], [20] Depending on the spatial resolution and data averaging requirements, the camera does not need to operate at more than a few frames per second to achieve 1 cm resolution over a 40 m depth. It may be preferable to use a 'single shot' mode of the camera to collect data at the required intervals.

The next step for image processing is to automate it. Currently the image is analysed manually by loading it in ImageJ and using a built-in tools analyse and calculate pixel intensities at the positions of interest. The data is then taken and put into an Excel spreadsheet template which calculates and outputs the spectral plots. Programming developed to capture the image can be continued to process the image as well. For example: an image captured by the CCD can be read programmatically as a 2-dimensional matrix of values corresponding to the pixels. Since the filter wheel is fixed in position, the locations of each filter's output on the image are known and the appropriate pixels can be analysed. The calculations done by the Excel spreadsheet can also be carried out by the program, and it will likely be quicker and more computationally efficient. This would allow the fluorescence sensor controlled by a laptop or microprocessor and to be integrated with the rest of the Cone Penetration sensors.

### **3.7 Summary**

A fluorescence spectrometer has been developed for the purpose of contamination detection in soil. Typically, a spectrometer strives for the highest resolution, but the primary goal here was to create a very compact and portable one that could fit into a 25 mm diameter tube and have simple, robust optical alignment. The resolution required is whatever is sufficient to distinguish different spectra to be unique from one another. Therefore a scheme using the light intensity difference between long-pass filters of different cut-off wavelengths was developed as a spectrometer.

Since 5 filters were used in this design, the sensor output resulted in 4 wavelength ranges whose relative intensities described the fluorescence spectra. This gives a 4 point spectrum which has fairly

poor resolution compared with the conventional spectrometer. From the various fluorescence spectra tested here, it can be seen that the orange (602 nm peak wavelength) and green (513 nm peak wavelength) fluorescent papers have results that are distinguishable from the hydrocarbon samples. In particular, the green paper and pyrene have peaks that are about 30 nm apart, but have clearly distinguishable results because the peaks occur near the filter cut-off. In this way the filter wavelength ranges can be designed to target wavelength ranges of interest. Crude oil and MFT were also tested and were seen to have a much broader fluorescence spectrum with many peaks which suggest the complexity of its composition. The fluorescence efficiency was also investigated as comparison between excitation at 405 nm wavelength used here, and typical UV wavelengths from literature. The efficiency was found to be about two orders of magnitude less compared with UV excitation, although other factors such as solvent or lack thereof have an effect. Overall, this prototype device is capable of distinguishing between fluorescence spectra despite its resolution and a field test design was discussed to package it fully into its 1 inch diameter tubing for use in cone penetration.

## 4. Light Scatter Sensors:

This chapter will focus on Light Scatter as a method of characterising slurries and three devices developed to analyse slurry samples under three different scenarios. Light scatter sensors are

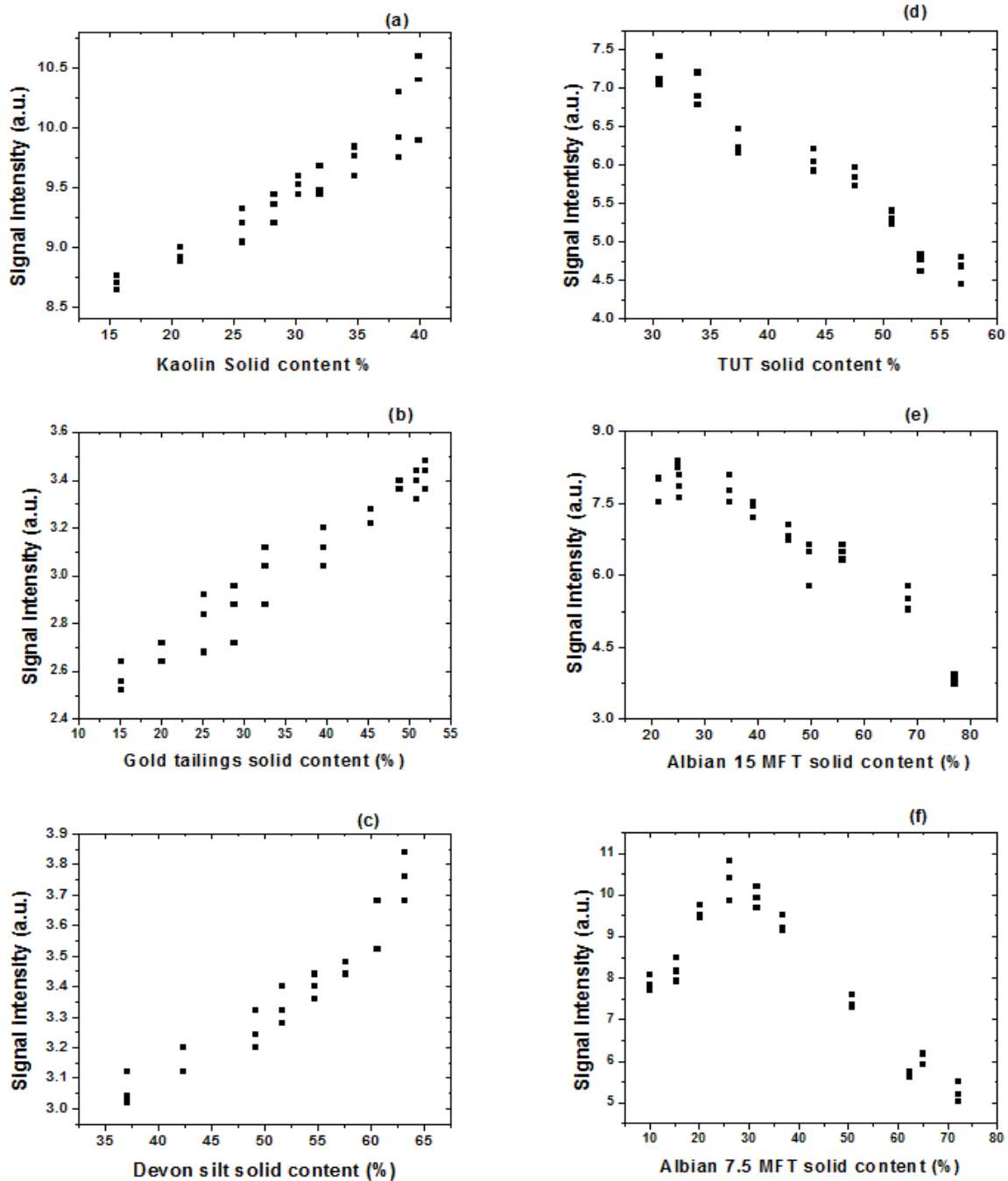


Figure 4-1 – Scatter signal measured with changing solid content % for (a) Kaolin, (b) Gold tailings, (c) Devon silt, (d) TUT, (e) AL15, and (f) AL7.5. Kaolin, Gold tailings and Devon show increase in signal with increasing solids content, but the MFT (d – f) show a somewhat reverse trend. [2]

available commercially to measure the size and concentration of particles in dilute solutions. [8], [9] Here, the goal is extend that to samples which are much more concentrated: >30% w/w. As discussed in previous sections, the scattering theory which must be used here is Mie Theory since the scattering particle and wavelength of light are of similar scale. Mie Theory simulation apps are widely available for single scatterer calculations, but high concentration requires a Finite-Difference Time-Domain simulation (or similar) to be used. An alternate method is to gather empirical data about the light scatter at various concentrations to create a fit or calibration. Various samples were measured before this work to find a relationship between signal intensity and solid content %. [2] The measurements in Figure 4-1 a – c are of non-oil-affected samples and show increasing scatter signal with increasing solids content. The other three samples (d-f) are oil sands process affected tailings and show a reverse trend. Given these experiments, light scatter is capable of measuring change in solids content, and a device was developed to measure at several locations simultaneously.

## 4.1 Stationary Cylinder:

### 4.1.1 Design

A device prototype was set up to measure the solids content of a sample based on light scatter. Incident light on the sample would be scattered and detected by a photodiode. In general the amount of scattered light is proportional to the concentration of scatterers which related to the solids content of the sample. A test cylinder of 50 cm x 18 cm diameter made of transparent acrylic was used to hold the sample. Then a rectangular aluminium rod with a foldable flap was fabricated to hold the sensory instrumentation. Locations for photodiodes were machined along the main

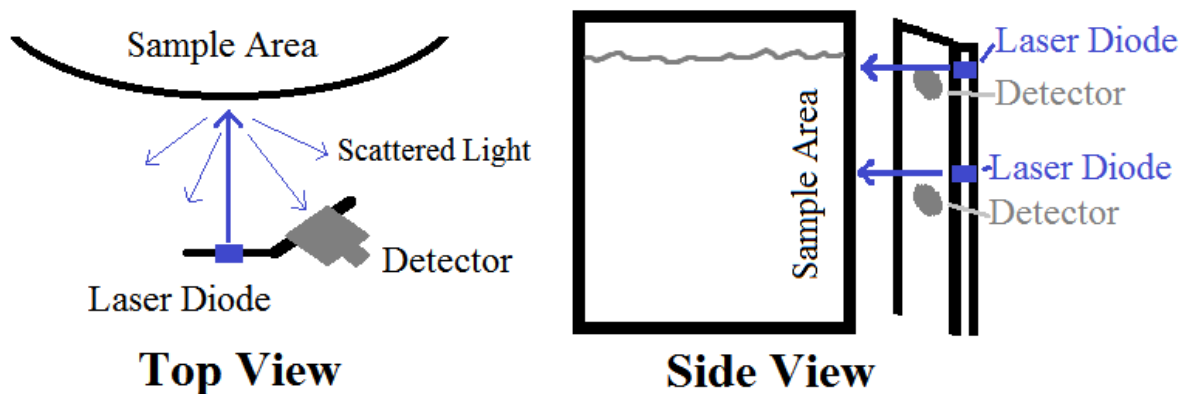


Figure 4-2 – Schematic of laser diode and photodiode arrangement. There is a 20° angle between the laser diode and photodiode, and they are spaced 1 cm apart vertically.

supporting rod every 2.5 cm and locations for laser diodes were machined on the adjacent flap. To avoid reflected light interfering with the scattered light in the photodiodes, the laser diodes were set up perpendicular to the surface of the cylinder and offset 1 cm above the photodiodes which were positioned at a 20° angle from the laser diode beam path as in Figure 4-2. This angle was chosen as a compromise since placing the photodiode at a smaller angle typically increases the signal (scattered light), but too small of an angle leads to noise from light reflected off the surface of the cylinder.

Previous work had been done in the lab group to design and to implement a simple square wave generator op-amp circuit to drive and pulse the laser diodes. This was used in the initial testing of the sensor. A disadvantage of this implementation is that the laser diodes were operated in constant voltage mode. Since a laser diode's output power is proportional to the current driving it, and since the laser diode has a non-linear current-voltage response, very small changes in voltage result in large changes in current and hence output power. Therefore it is very difficult to set and maintain a constant output from the laser.

A laser diode pulsing circuit was then designed using a commercial laser driver integrated circuit: FL500 from Team Wavelength. It is a constant current controller capable of driving up to 500 mA with a linear voltage controlled setpoint. The laser diode used was a 405 nm typically operated

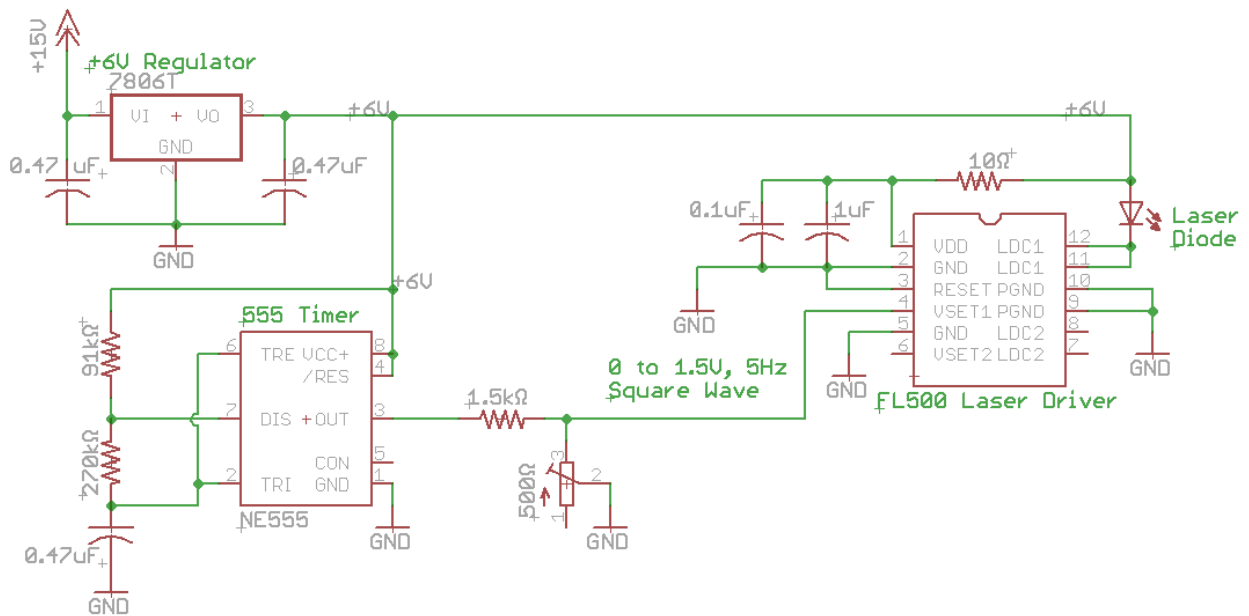


Figure 4-3 – Laser pulsing circuit. Top left: voltage regulator; bottom left: square pulse generator; right: laser driver IC

around 20 mW. The laser pulsing circuit was designed using a 555 timer to create a square wave signal with a frequency of 5 Hz and a voltage divider with a potentiometer was used to create an adjustable input signal to control the current flow through the laser diode. The laser diode output power was kept approximately constant by maintaining a constant drive current. Pulsed operation is used in order to remove the background from the signal at the time of measurement.

The photodiodes were connected directly to a Tektronix two-channel oscilloscope to display the signal in real time. Initially, four photodiodes were used in the setup and a switch box was used to select a photodiode. The output would then be displayed and the peak-to-peak signal, which is calculated internally, was recorded manually from the oscilloscope. The settling rate of the sample used was typically slow enough that measurements would be taken every couple minutes for the initial period, then anywhere from every hour to twice a day afterwards depending on the sample type. Since samples with higher initial solids content settled very slowly and were measured over the period of a month, measurements were only taken twice a day. However, as lower starting solids content samples were used, more frequent measurements were required which made it difficult to continue taking manual measurements. The setup was modified to use two oscilloscopes, each with two channels, and then automated with LabVIEW to record data with a specified time interval ranging from a few seconds to 30 minutes.

Another issue that occurred with the previous setup was that the laser diodes did not have constant output power relative to each other. Even when using the new driving circuit, laser diodes can have different current to output power efficiencies as well as different optical power output due to heating. Therefore a 'beam-splitter' design was used whose main purpose was to help maintain consistency between the levels. If the output of the laser diode decreased due to heating, it would affect all the levels at the same time and thus it would be easier to determine as a diode effect and not a real signal. One laser diode was pointed downwards at the top of a vertically

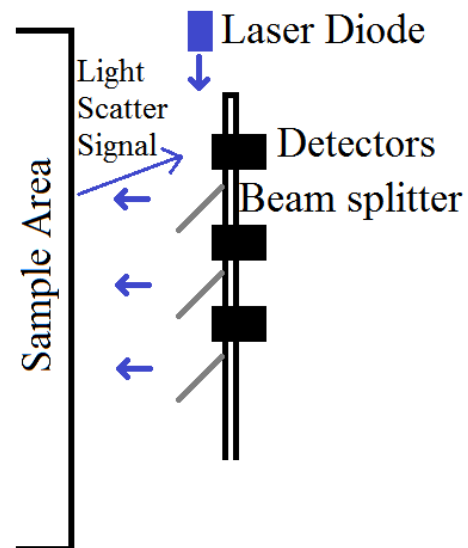


Figure 4-4 – Schematic of beam-splitter design. Laser diode emits downward and the beam-splitters redirect a part of the beam horizontally.

aligned series of 1 mm thick microscope slide pieces which were placed at a 45° angle to reflect the light horizontally. These were arranged to be at the same location as the previous positions of the laser diodes and the flap supporting the photodiodes was again placed at 20° to the incident light. The light reflected and transmitted at each beam-splitter can be calculated using the Fresnel equations for reflection and transmission if the polarization is known. Since the measurements use the relative change in signal from the initial state is used to determine the change in solid content, the purpose of the beam-splitter design was to maintain consistency between light sources. If the output of the laser diode fluctuated, it would be apparent in all of the levels and not mistaken for a real signal.

#### 4.1.2 Results:

The simplest material tested was Kaolinite (or Kaolin), a type of white or beige powdered aluminum silicate clay, mixed with water. Kaolin is a common type of clay found all over the world and is a large part of the soil composition in Northern Alberta. [1] Dry Kaolin powder was mixed with water to make 33% solids content slurry which is the mass of solids divided by the total mass and the initial height of the sample was 19 cm. Four measurement heights were used: 18 cm, 15.5 cm, 10.5 cm, and 1 cm named CH1, CH2, CH4 and CH6 respectively. Due to CH2 being close (2.5 cm) to CH1, it was noted that the light scatter from CH2's laser spot would be detected by CH1's photodiode. Therefore, it was put on a different supporting rod (with a separate laser diode) and placed about 90°

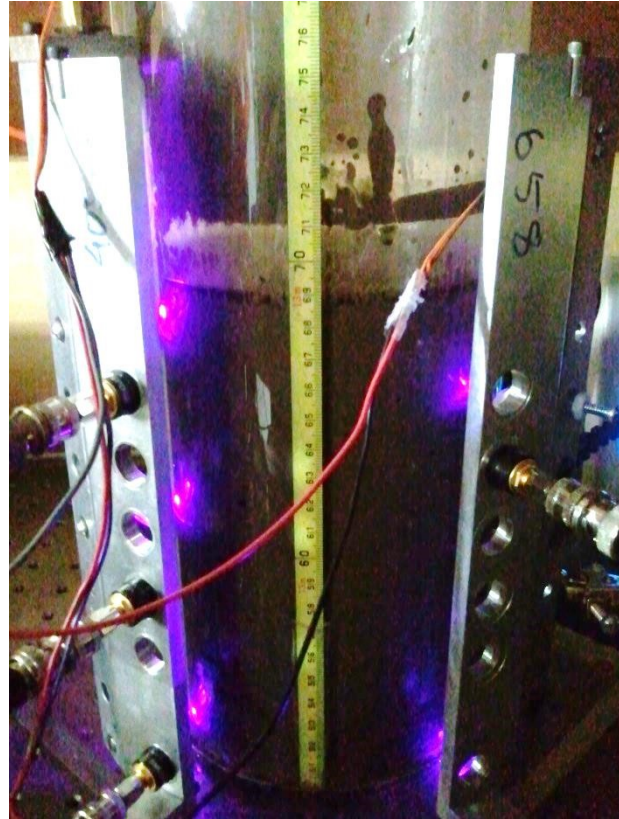


Figure 4-5 – Example setup with TUT % sample. Left side, top to bottom CH1, CH4, CH6 and right side CH2.

away to avoid signal interference from CH1. The separation between CH1, CH4 and CH6 was sufficient and there was no noticeable interference. Measurements were automatically recorded approximately once per minute and the measurement was carried out over 3 days. The scatter angle measured was 20° backscatter.

During settling the solids move down the cylinder leaving a visually abrupt 'solids line' with solids below and clear water above. Measurements at the 4 different heights of the sample show the light scatter intensity decreasing corresponding to the decrease in solid content at that particular height in the sample and observing during the settling shows that the drop in signal does coincide with the solids line at the height of the laser spot. The lowest two

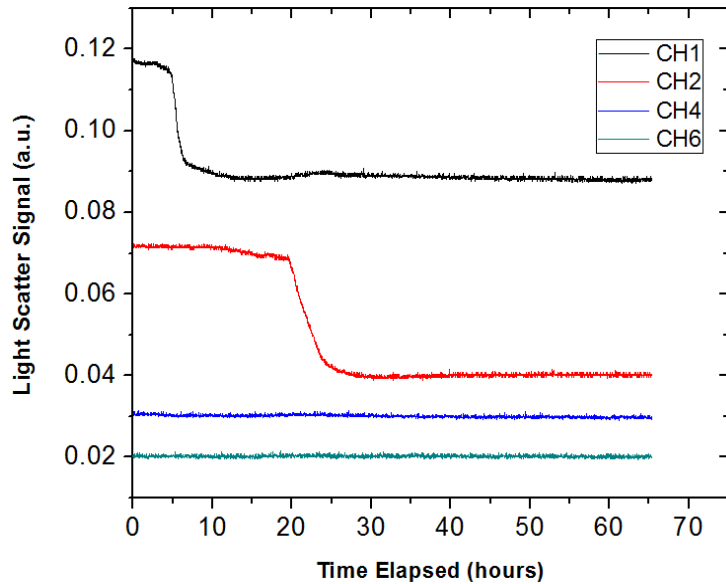
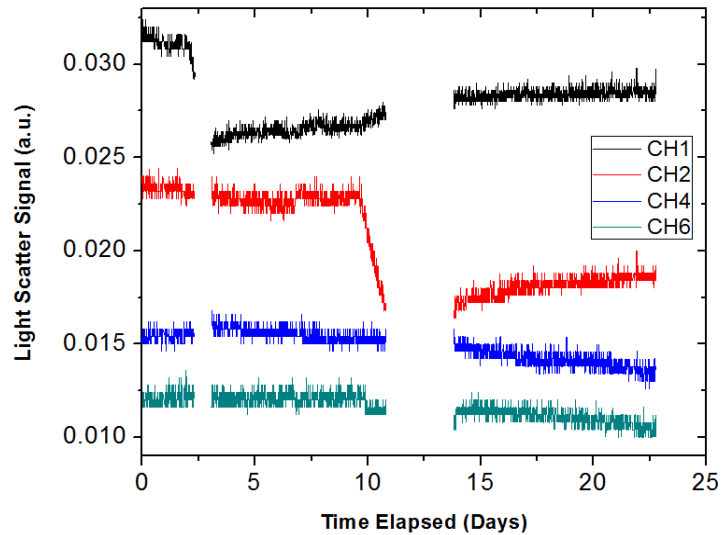


Figure 4-6 – Kaolin 33% starting solids content of hours elapsed versus relative signal strength. Measurement heights at 18 cm, 15.5cm, 10.5 cm and 1 cm for CH1 through CH6 respectively and measurement angle was at 20° backscatter.

measurement heights do not decrease because they are much farther down the cylinder. It is expected that there is a slight increase in the solids content which may be too small to be noticed by the sensor. For example, the total height of the sample at the start of measurement was 19 cm and it settled to final height of 15 cm so that there was 4 cm of water at the top. If it is naively assumed that the solids which settled out from that section is evenly distributed to the rest of the sample, the solids content would increase from 33% to 38% in this case. However, the lower portion is also settling therefore it is more likely that more of the increase occurs at the very bottom of the cylinder. While relatively straightforward to calculate the settling of a free particle (dilute samples) for slurry with higher concentrations it becomes more difficult. The bottommost sensor at a height of 1 cm is the lowest possible with this setup due to the silicone sealing which makes a watertight joint between the acrylic cylinder and its base. It is possible a sensor closer to the bottom of the cylinder will detect the increase in solids.

The setup was then used to measure oil sands tailings samples of Thickened Underflow Tailing (TUT) (also at 20° backscatter) which are a much more complex system containing sand and clay coated with bitumen and mixed with water. This sample settled more slowly so measurements were automatically taken every 10 minutes over the 1 month measurement period. The first 18 hour gap of data was due to the signal level dropping below the trigger level; this was corrected and the measurement continued. The second gap of data was due to a power outage which stopped the

data measurement over the weekend. As this sample settled, it gave a similar response but appeared noisier compared to the Kaolin sample. Part of the cause is a decreased signal due to the dark colouring of TUT, and thus a decrease in the signal to noise ratio. The Kaolin sample is whitish in colour whereas the TUT is a dark grey which is much more absorbing. The laser power was increased to compensate however it was near the maximum output of the laser diode



**Figure 4-7 – TUT 35% starting solids content measured over 23 day settling. Measurement heights at 18 cm, 15.5cm, 10.5 cm and 1 cm for CH1 through CH6 respectively and measurement angle was at 20° backscatter. Two gaps in data are due to an error in data collection trigger and a power outage.**

and it has been noticed previously that light at high intensities can cause changes in the sample at the laser spot. Since the wavelength used is near UV wavelengths (405 nm) it may have high enough photon energy to alter chemical bonds. Additionally it was observed that over a couple days algae would begin to grow around the laser spot. Algae were also observed when samples were left exposed to room light for several days. Another cause for the ‘noisy’ appearance is that the complex composition of the slurry has particles and bitumen droplets which cause fluctuations in the signal as they pass by compared to the relatively homogeneous Kaolin sample. The light scatter signal slowly increased in both CH1 and CH2 after the signature decreases in signal due to settling of the solids line past the detector. It was observed that for oil sands tailings samples the water at the top of the slurry would have particulates floating in it. As particles with higher density than water settled, others with lower density, such as oil droplets, should rise, and these particulates would scatter light. The two lower sensors (CH4 and CH6) were seen to decrease over the course of the measurement. One possible explanation for this is that larger particles settle faster than smaller ones; therefore, if they leave the region being measured, the light scatter they contribute would be gone.

## 4.2 Calibration Ring:

This measurement scheme allows for the relative change in light intensity to be measured as the solids content of the sample changes but does not exactly determine the concentration. Mie theory is typically applied to a single spherical scatterer for the simulations which are widely available. Since the samples are typically >30% solids content or approximately  $5 \times 10^7$  particles per mL (at  $10 \mu\text{m}$ ), this case deviates from a single



Figure 4-8 – A microscope picture taken of Kaolin powder showing range of particle sizes and irregularity of shape.

scatterer case as it is much more concentrated. Additionally, the scatterer is typically an irregular shape as seen in Figure 4-8 and there is a distribution in the particle sizes which varies with different samples. The microscope sample shown was prepared by mixing some Kaolin powder with water and allowing a drop to dry on a glass microscope slide. In order to accurately simulate the response a more complex simulation would need to be carried out especially to address high concentration and size distribution. Alternatively, the samples can be progressively diluted and measured to empirically find what the relative change in light scattered intensity is when there is a change in solid content. The single spherical scatterer Mie simulations can still be used to help gain an understanding of the general behaviour of the light scatter intensity.

### 4.2.1 Design:

To accomplish this calibration measurement, a ring was cut out of a 9.5 inch diameter, 0.5 inch thick PVC pipe. The setup is shown in Figure 4-9. A hole for an incident laser diode was made, located at 12 o'clock in the figure, and the laser diode is focussed onto the sample from outside the ring. Threaded holes were cut for photodiode detectors up to  $90^\circ$  both clockwise and counter-clockwise from diode's location. Additional larger holes were made to view side-scatter patterns with a CCD camera for other studies. A sample would be placed at the center of the ring in a cuvette, and the laser would be focussed on the surface of the cuvette. The backscattered light can be measured at the various angles up to  $90^\circ$ . Due to logistics of setting up and carrying out the measurement, only 8 angles would be monitored at a time. Angles could be changed as required, but typically four angles

would be chosen on either side of the laser with one angle (45° and/or 20°) repeated on both sides for comparison. In particular the 20° angle was most important because it was the angle chosen for solids content settling measurements since it provided a good compromise of high signal and avoidance of specular reflection.

The laser driver used was an FL593 USB controllable board from Team Wavelength which utilizes the same

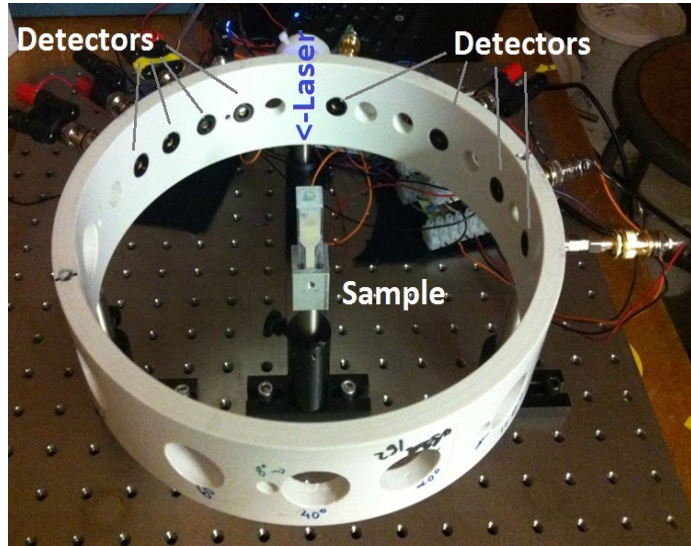


Figure 4-9 – Calibration ring setup. Focussed laser diode enters at 12 o'clock on this schematic and 4 detectors are positioned on either side of the laser diode.

FL500 chip used previously. Data acquisition was handled by a National Instruments DAQ USB-6008. The DAQ has 8 12-bit analog inputs with a voltage range of  $\pm 10$  V and can read from all inputs simultaneously. A transimpedance amplifier was also designed with a gain of 200 mV/nA to convert the photodiode signal into an appropriate voltage range for the DAQ. Taking advantage of the USB control capabilities of the laser diode driver, a LabVIEW program was written to pulse the laser diode, then read and save the data.

#### 4.2.2 Kaolin & Tailings:

Kaolin was available as a dry powder, so the highest solid content possible was limited by the ability to physically prepare the sample. Collaborators from Civil and Environmental Engineering who supplied the Kaolin reported the particle size distribution to lie mostly in the 1  $\mu\text{m}$  to 20  $\mu\text{m}$  range. The tailings slurries were already mixed with water, so the maximum concentration was the initial concentration, which was typically 50%. The starting sample was then diluted by mixing it with deionized water. When diluting the tailings, care was taken to thoroughly mix the starting sample because as the mixture became more dilute, the larger particles settled out in a few seconds. Likewise, when the measurement was carried out the cuvettes were agitated right before measurement.

Backscatter angular measurements are shown for various solid content mixtures of Kaolin powder using a 405 nm wavelength laser diode as the source. The 20° backscatter was chosen for the sensor design because it gives a compromise between high light scatter signal – expected to

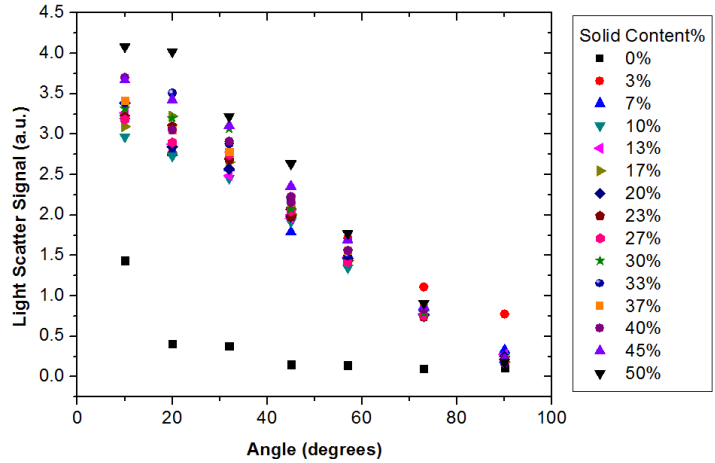


Figure 4-10 – Light scatter signal change depending on angle for different solid content mixtures of Kaolin. The source used was a 405 nm wavelength laser diode.

depend on  $\cos(\theta)$  – but avoids specular reflection close to 0°. These measurements were fit and show that

the light scatter is proportional to  $\cos^{-1.5}(\theta)$  for non-zero solid content. The measurements at 10° do not appear to show much specular reflection interference except for the 0% s.c. sample; therefore, to be completely safe, 20° is a good choice to be the measurement angle. It still has similar signal strength compared with 10° and is less likely to experience interference from specular reflection.

Change in light scatter signal with solid content was analysed by looking at 20° backscatter from the previous measurement. The change in light scatter was found to be an initial sharp increase and

then a slow increase onwards which was typical for both Kaolin and tailings samples. The sharp increase is interpreted as the dilute regime where each additional particle is fully illuminated and thus contribute maximum scatter. The slow increase is interpreted as when the suspension becomes concentrated enough that additional particles begin to screen one another, which decreases their individual contribution. This data is fitted as two linear parts. Using this calibration, the relative change in

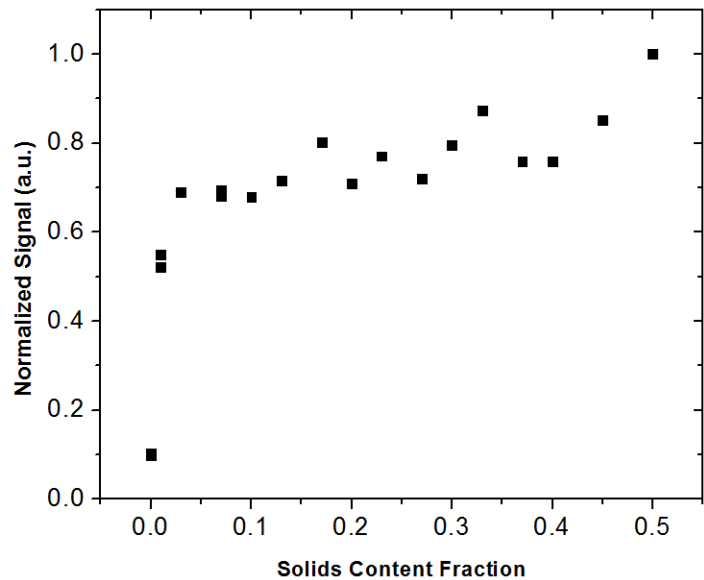


Figure 4-11 – Kaolin calibration measured at 20° backscatter and 405 nm source. Various concentrations were made and measured to find the relative change in signal with solids content. The shape of the plot is typical for both Kaolin and various tailings samples.

signal can be used to find the corresponding change in solids content.

#### 4.2.3 Flow Sensor Sample:

A dry sample was supplied for calibration and testing which is being used for initial testing in the flow sensor project. The majority of the mass contribution was from 100  $\mu\text{m}$  to 300  $\mu\text{m}$  range particle diameters which were spherical beads. Smaller particles were also present which were crushed sands and irregular in shape. The relatively large particle sizes caused dilutions below 60% to settle very rapidly, making measurement near impossible. Therefore this sample was instead diluted in a saturated salt solution in attempt to increase the density of the solution because the settling velocity is proportional to the difference in density of the particle and the medium. Table salt was added to deionized water in a 20mL beaker until the crystals no longer dissolved. The solution was allowed to settle for several minutes and solution was taken from the upper part of the beaker when preparing the samples. A sample of just salt water or 0% solids content was compared with deionized water with the laser diode operating at 55 mA. The salt solution had an average signal of  $0.51 \pm 0.06$  mV compared to the deionized water with  $0.44 \pm 2$  mV, so they have very similar scatter. The error arises from the variation in signal over 4 measurements and is largely due to the reliability of positioning the cuvette. This sample was prepared in 10% increments from 0% to 100%.

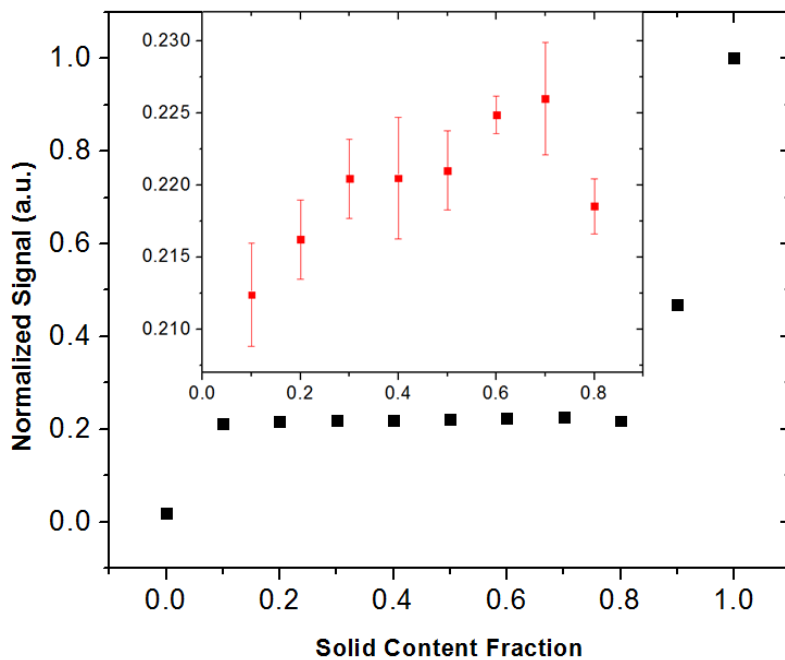


Figure 4-12 - Measurement of the backscatter signal at 20° with 405 nm wavelength source of sandy sample diluted in saturated salt solution. Samples at 90% and 100% did not have enough water to be fully wetted.

The results from 90% give a different result because there was not enough water to wet the whole sample. This sample had air gaps which was visible by the grainy texture of the sands as opposed to particles suspended in a liquid which were more mud-like. This is also true for the 100% sample as it is completely dry. As discussed in the theory section, the air gaps, or an air medium has lower index of

refraction compared with water. Since the amount of light scattered depends on the contrast between the particle and medium, the driest sample scatters more light as expected. Dilutions between 0% and 10% were not measurable because the particle settled too quickly.

The signal response of this sample is similar to that of Kaolin. After several measurements, the average signal is plotted, and the error comes from the deviation of the measurements. The sample must be shaken and repositioned before settling reoccurs. In this sample, as the amount of solids increase past 70%, the signal begins to decrease. For particles suspended in a medium, light incident on a particle will reflect when entering and exiting it and the amount of light reflected depends on the difference in index of refraction. When the particles begin to be packed extremely closely, the light may be able to pass between particles with similar index of refraction without crossing through water which has much lower index of refraction until it is absorbed. This would explain a decrease in signal. Additionally, this occurs around 80% w/w concentration and if the density of the solids is approximately  $1.5 \text{ g/cm}^3$ , this would lead to a concentration of 73% v/v which is close to the theoretical limit of 74% for spherical packing. The increase at 90% is due to the sample becoming a grainy solid (like wet sand) with air gaps instead grains completely immersed in fluid. The air gaps occur because the particles have some maximum packing factor and eventually there is not enough water to fill the voids. The 100% (dry) sample is expected to have the highest scatter for the same reasons. Visually it also has a pale colour compared to the water-darkened samples.

#### 4.2.4 Polystyrene Beads:

To learn about the effect of particle diameter on light scatter signal in a multiple scatterer environment, testing was carried out using polystyrene microspheres (or beads) from PolySciences. [21] The beads were available in a range of sizes from 50 nm to 90  $\mu\text{m}$  and were available as a 2.5% w/v aqueous solution. Two drops were diluted with just enough water to carry out measurements; care was taken to preserve the w/w concentration and

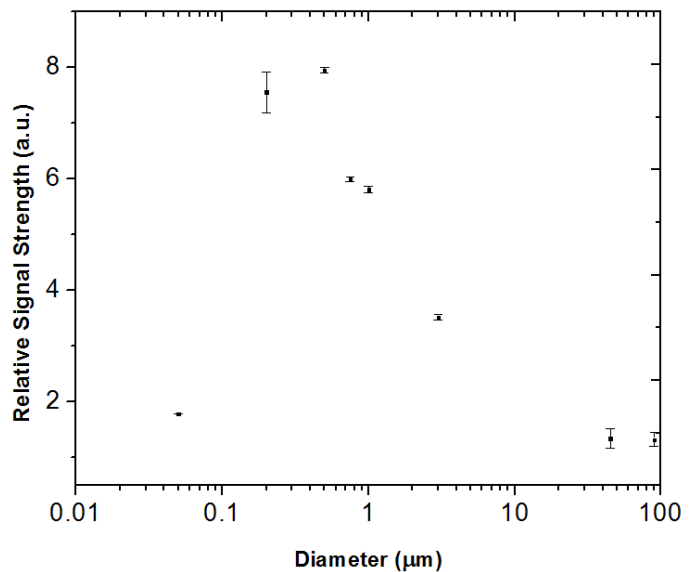


Figure 4-13 – Light scatter from various diameters of polystyrene beads in 0.1% w/w aqueous solution, measured at 20° backscatter with 405 nm wavelength source.

approximately 1.5 mL of water was added in each. The final concentration of the samples was 0.1% w/w. The goal of the test was to measure the change in light scatter with respect to particle diameter for 'concentrated' solutions so the solids content of the samples were fixed. The samples were measured with 405 nm wavelength laser diode at 20° backscatter.

Each sample was measured a couple times at 20° both clockwise and counter-clockwise. The spread in values gives the error shown. It was found that the amount of light scattered initially increases with diameter to a maximum at 500 nm, then drops as the diameter continues to increase. The initial part behaves like single sphere simulations with increase in diameter corresponding to increase in scatter. The latter part decreases because while the weight concentration is constant, the number of particles per unit volume (particle concentration) varies. For a fixed mass of solids, the number of spherical particles is proportional to  $r^{-3}$  so the particle concentration decreases rapidly as the diameter becomes larger. The initial part is in the regime where there are so many particles that additional ones do not affect the amount of light scattered back by much, whereas the latter part enters regime where each particle contributes strongly to the amount of light scattered.

The main purpose of the device is to determine the solids content from amount of light scattered. The particle size is expected to affect the amount of light scattered based on single scatter simulations, however another effect which occurs is that the size of the particle also dictates how many particles are present for a given solids content and it dominates as the particle size gets larger. There is some critical diameter where the particle concentration decreases to the point where it is no longer in the multiple scatter regime, and here it is around 500 nm. It is expected that if the solids content is higher, this critical diameter will also be higher because the particle concentration will be sufficiently high even at larger diameters. These effects will affect how the light scatter intensity will behave and present a problem in increasing the complexity of analysing the solids content, but also offer the opportunity to gain particle size information from the data.

### 4.3 Centrifuge Sensor:

The settling rate of a free particle is proportional to the acceleration due to gravity. This has been evaluated by oil companies with a prototype to speed up the settling rate of the tailings with promising results. [1] One requirement for using this technique commercially is the centrifuge parameters of how long to run and what acceleration is needed. For example in a centrifuge setting, fluids are much easier to transport in large amounts than solids, so the centrifuge needs to be stopped when just enough settling has occurred. Additionally, the centrifuge uses a relatively large amount of power and consumption should be minimized. Since the composition of the tailings has a tendency to vary, the tailings should be monitored in-situ. Centrifuge compatible cameras can be used to visually monitor the progress of the settling, but measurement of the solids content would reveal more data and would, for example, give better indication for a stopping point.

#### 4.3.1 Design:

This system was applied to a design for measuring a cylinder which would be placed inside a centrifuge at 100 times the gravitational acceleration. Various samples including Kaolin and different tailings would be tested. The same laser driver circuit was used as shown previously in Figure 4-3. The laser diode would be pulsed at a rate of 5 Hz and a potentiometer could be used to change the intensity of the laser. For detection, the same silicon photodiodes were used and a data acquisition card built in with the centrifuge would be used. Therefore a transimpedance amplifier was designed with a TL074 operational amplifier (op-amp) to convert the photodiode current signal into an acceptable voltage range. The gain chosen was -200 mV/nA for an output voltage range of 0 to -10 V given the typical response of the photodiode. The photodiodes available were cathode grounded which gives a negative voltage signal with the transimpedance amplifier. Since there is no high speed operation, the photodiode was not reverse-biased in favour of having a lower dark current.



Figure 4-14 – Centrifuge sensor. Signal amplifiers on perforated board at left, and laser diode driver on perforated board at top. Detectors covered by bandpass filters at center, and glass beam splitters at right.

The sensor built used the beam splitter design. One 405 nm wavelength laser diode was directed vertically downwards through 6 beam splitters which redirected a portion of the beam horizontally. The beam splitters were 1 mm thick glass microscope slides. Two different spacing of beam splitters were used (1 cm and 2 cm) in anticipation of different sample amounts to be tested. The beam splitters were positioned along the main aluminum rod with the detectors on an adjustable ‘detector flaps’ similar to the stationary cylinder. For the 1 cm spacing, two flaps on either side of the beam splitters were needed because the diameter of the photodiode was 1.3 cm. The signal amplification circuitry was built on a perforated board and clamped to the detector flap. The laser driver circuitry, also built on perforated board, was mounted above the device with the laser diode holder.

All of the electronic components were first tested in a small centrifuge and functioned normally after removal. The entire sensor was also tested for good health between centrifuge measurements and no problems were detected. The perforated board used is 1/16” thick and is made of glass fibre-reinforced epoxy laminate sheet, which also has good mechanical properties. A back of envelope calculation found that the board was more than 3 times stronger than required. An aluminum box with ¼” thick walls was also built to house the sensor to protect it in case of accidents or to contain the pieces if it were to break apart.

### 4.3.2 Testing & Results:

Before going to the centrifuge, an initial test was carried out with the device sitting stationary in front of a cylinder to measure Kaolin settling. [2] The detector flaps were adjusted to measure 20° light scatter. A 2-channel oscilloscope was used for the data acquisition with alternating levels connected through two switchboxes (1, 3, 5 and 2, 4, 6). First the upper two photodiodes were connected (1 & 2). When the solids had settled past the first two detectors the first detector, CH1, was switched to photodiode 3

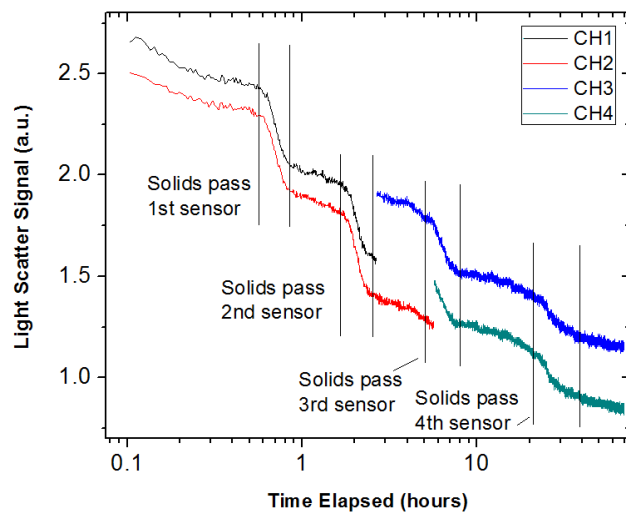
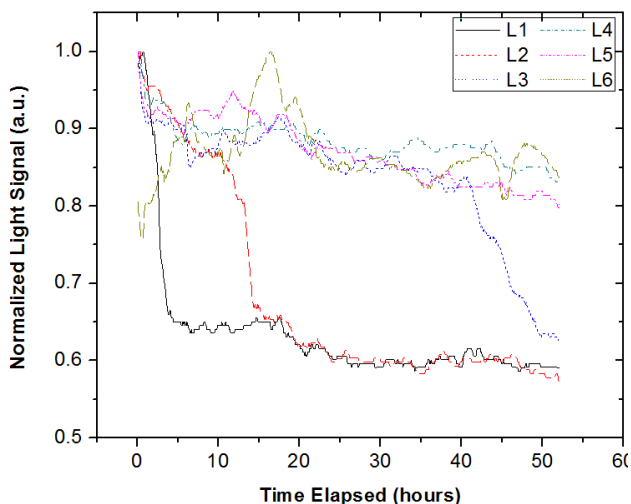


Figure 4-15 – Device test verifying the performance of the sensor using 405 nm wavelength source and measuring at 20°. The neighbouring detectors interfere with the signal.

(CH3). Likewise when the solids settled past the 2<sup>nd</sup> detector and was approaching the 3<sup>rd</sup>, it was switched to detector 4. After 70 hours the solids line had passed photodiode 4 and the measurement was stopped. When cross-referencing with the visual progress of the solids line, the first decrease in signal occurs when the solids passes the first laser spot, the second at the second laser spot, and so on. However, the signals of the photodiodes are clearly affected by their neighbours. This is expected because the sensor locations are much closer to each other in this design; the beamsplitters are spaced 2 cm apart, and due to alignment of the beamsplitters, the laser spots when they hit the sample are 1.85 cm apart.

During initial testing in the centrifuge, it was discovered that the ambient light would saturate the detector and the ambient lighting was required for other measurements being performed such as for a camera to visually track the settling progress of the solids. An interference band-pass filter from Anchor Optics with 10 nm FWHM centered at 405 nm was used to eliminate the unwanted light. A bracket holding 6 of these 1 cm diameter filters was screwed onto the detector flap. The interference filter is specified for normal incidence. For an interference filter, as the angle of incidence increases from normal, the pass band shifts to shorter wavelengths which was measured and verified for these filters. The ambient lighting is white light LEDs which has an emission peak around 465 nm with a phosphor providing longer wavelengths. The filter was measured in a Perkin-Elmer NIR-UV Spectrophotometer for normal, 10°, 20°, and 30° angles of incidence. Since the pass band shift to higher wavelengths with increase angle, the filter sufficiently blocks out all ambient light. The transmission of the 403 nm to 407 nm range drops to around 1% at 20° so it will block off-angle light from other sensors with proper distance from the sensor to the sample. The real signal will not be affected because the detectors are on an adjustable flap, as seen in Figure 4-14, which is rotated so that the detectors are normal to the incoming light.

Data was taken for a centrifuge run using



**Figure 4-16 – Normalised signal of MFT in centrifuge run at 60g. Light signal decreases to around 0.6 once the solids have settled below that level and water remains. The solids settle below the first 3 levels after 50 hours. Colour available in electronic version.**

mature fine tailings (MFT) with an initial solids content of 46.6% measured by gravimetric method, and the centrifuge was run at an acceleration of 60 g with the detectors at 20° to the incident light. The top-most laser spot was at a height of 12.6 cm above the base, with subsequent laser spots separated by 1.85 cm. The top three sensors detected the solids line passing by the sensor and the midpoint of the step was used to find the time it occurred. Using this, the height of the solids could be determined at those 3 times, which all corresponded with the height of the solids at those times as measured by the camera. The solids do not settle past the lower three sensors and therefore those signals remain high.

The sensor was designed to have a 5 Hz square wave laser pulse to measure the peak-to-peak value as the signal and remove the background. This was used with the oscilloscope; however the data acquisition at the centrifuge only sampled data once every minute. Since the sampling was much less frequent than the pulse of the laser, the data did not have a shape that was easy to analyse, but there were enough data points that the overall shape of the signal was apparent. The maximum and minimum of the signal over time were extracted from the data by tracing the contour of the signal. This contributes most of the noise in the resulting data.

In principle, using a fit made with the calibration ring, the normalised light scatter signal can be converted to represent the solids content of the sample. At the time of writing, the density profile change over time was not available to compare against, but in general it reflects the solids settling past the top 3 sensors and the bottom 3 sensors remaining with solids.

### **4.3.3 Summary**

The sensor was successfully operated under high gravity and the height of the solids settling line was tracked correctly as compared to pictures taken by the camera. The behaviour of the signals are as expected based on stationary cylinder measurements and can be compared with other measurement methods of the solids content as they are available in the future. Optimization of the data acquisition would improve the noise and reliability of the sensor.

## 4.4 Insertion Sensor:

An opportunity arose to test the light scattering sensor in collaboration with Total E&P at a Saskatchewan Research Council facility in Saskatoon, Saskatchewan. Gamma ray measurements were carried out on the sample to determine the solid content with respect to height each month, and at the middle and end of the measurement, samples were also physically taken. The light scatter sensor was designed into an insertion sensor for a 3 m tall tank to measure the settling progress of oil sands tailings sample with flocculent over the span of a year and could then be compared with the measurements taken by the gamma ray method.

### 4.4.1 Design

#### *Housing*

The device was encased in a 2.25" inner diameter cylindrical acrylic tube with sensors at levels coincident to the other measurements being carried out. Twenty positions were monitored spaced 10 cm or 20 cm apart based on information received about where those measurements would be taken. Blue (405

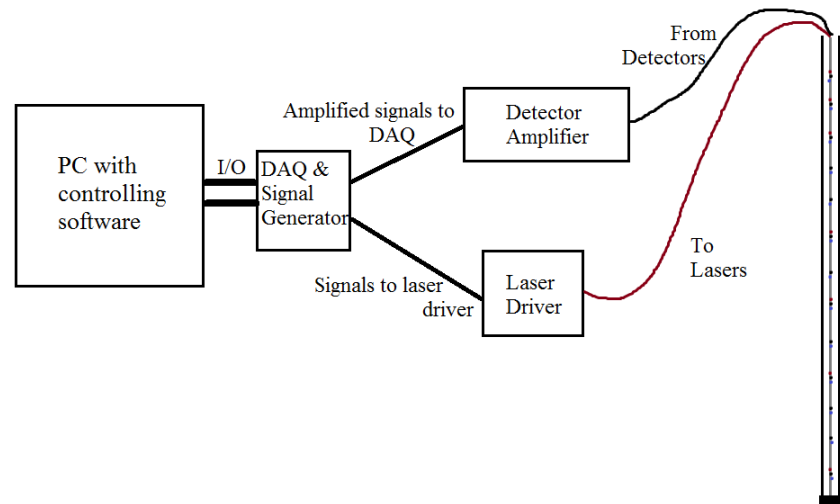


Figure 4-17 – Schematic of the sensor. The PC is connected with the sensors through USB hubs and controls the laser driver card. Signals from the sensors are amplified and then read by the data acquisition (DAQ) into the software to be logged and plotted.

nm) laser diodes were used at each level monitored and red (658 nm) were used at only 7 of the levels due to logistical constraints. The laser diodes and detectors were mounted on a 1" wide aluminum rod, fabricated in 3 sections by the in-house machine shop, which would be inserted into the acrylic tube and support all of the necessary wiring. Polycarbonate strips 1 cm wide were bent into loops and used to hold the aluminum rod uniformly against the surface of the tube. Since the laser diode would be very close to the surface of the tube no lens was used to collimate it. However, the tube had an inner diameter of 2.25" which was small enough that the reflected light would be focused onto the detector. Therefore, rectangular windows were cut into the side of the tube to

provide a flat surface. The ledges above and below the window were ground so that they would not collect sediment as the slurry settled. The tube would be inserted into the slurry and a cover would be placed on the tank, so the sensors would not be affected by ambient room light. The sensor tube was expected to float based on its volume and weight, so a magnet rated at 10 kg was inset on the bottom of the tube and a steel rectangular torus weight, about 3 kg, was made to wrap around the bottom of the sensor rod, with a cut out for the bottom most window. Finally, during installation, a clamp was used to secure the top of the tube to prevent it from moving.

### ***Electronics & Software***

The beam splitter design was not used here because of the sheer number of sensors and the difficulty of aligning the beam across 3 m. The laser diodes were driven using a USB controlled version of the previously used laser driver chip: FL593 from Team Wavelength. Each board supported two laser diodes so 14 boards were connected into two USB hubs connected to the controlling laptop. The FL593 board came with software which is capable of using setpoints to drive the lasers with constant current or constant power. Using the constant power mode would have been ideal, however due to time constraints and laser diode availability constant current mode was used. The available laser diodes did not have the built-in feedback photodiode necessary for constant power mode.

The same photodiode and transimpedance amplifier as in the centrifuge project were used as the detecting circuit. The photodiode was not reverse-biased because of low frequency operation (0.5 Hz). The amplifier gain was -200 mV/nA to give an output in the range of 0 to -10V. Cathode grounded photodiodes were used, which gives a negative voltage signal. The data acquisition card used was a National Instruments DAQ USB-6008 which had 8 analog single-ended inputs; therefore 3 data acquisition cards were also connected to the controlling laptop though the USB

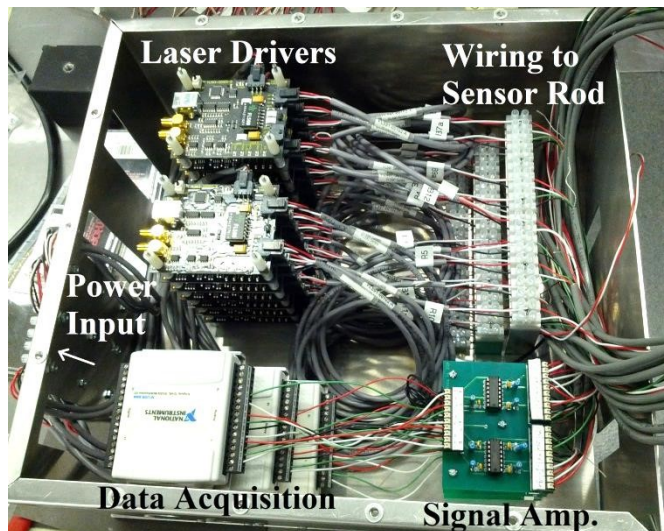


**Figure 4-18 – Electronics box containing laser driver, data acquisition and signal amplifiers. Power input screw terminals are mounted outside the box on the left. Slots have been cut on the left and right sides to allow wiring to exit the box.**

hubs. The detector circuits were designed with Eagle CAD and manufactured into PCBs (printed circuit boards) by AP Circuits. Each board was made to support 8 detectors and the outputs were arranged to feed into the NI DAQ with minimal hassle.

An aluminum 33 x 34 x 15 cm 'electronics box' which was fabricated by the machine shop was designed to organize and connect all of the laser driver cards, amplifier boards and data acquisition cards. The laser driver cards and amplifier boards required external power which was provided by a dual rail supply with max 0.5 A set at  $\pm 15$  V for the amplifier boards and a variable supply with max 5 A set at 6.5 V for the laser driver cards. The outputs and input to and from the laser diodes and photodiodes were organized and ended in screw terminals for easy connection with the wires from the sensor rod. The USB hubs were mounted on top cover of the box. After testing continuously for a couple weeks, it was found that the box dissipated its own heat and a cooling fan was not required.

The software to run the sensor was written with LabVIEW, a block diagram based programming language. LabVIEW was chosen because it is used frequently in research, various courses and by hobbyists. This means that there is a large support base available online to assist with learning it as well as implementing some tricky parts. Being a graphical programming language, it can be easier to debug and is easier to visualise the flow of programming for a programming novice. It is also geared towards and generally used for instrumentation purposes. LabVIEW has two main windows: the front panel and the block diagram where the coding is done. The front panel is basically a virtual instrument face and it allows for button and graphs to be placed and interacted with.

Since LabVIEW was being used to automate the data acquisition, custom control of the FL593 boards was implemented by creating a sub-VI (sub program) which bypassed the GUI and manipulated the setpoints of each of the laser driver boards directly. Since constant current mode was used, a warm-up time for the laser diodes was implemented because it was observed that the output power would drop slightly as the diode heated up during operation. Each time a measurement took place data was extracted from the laser driver board which had a built-in current monitoring resistor to log the laser current. It was observed that the current did not reach the setpoint (e.g. 30 mA for 40 mA setpoint) but that the current was consistent at the lower current with variation of around  $\pm 20$   $\mu$ A which was acceptable performance. During data acquisition, the laser diodes would be turned on, followed by 1 s of data collection at 10 Hz. Then the lasers would be turned off followed by another 1 s of data collection, thus creating the 0.5 Hz pulse. Initially

attempts were made to parallelize the pulsing of the laser diodes and the acquisition of the data, but the timing and order of the commands executed would change haphazardly. The acquisition of data was staggered into 3 measurements of blue laser diodes and 1 for red in order to avoid any light scatter interference from nearby sensors. In this way the two nearest sensors operating at the same time would be at least 20 cm apart. The raw data would be saved but also analyzed to find the peak-to-peak voltage which plotted on screen. The laptop used to run the sensor used 32-bit Windows XP because the laser driver cards were not compatible with 64-bit and more recent versions of windows would not recognize more than a couple of the laser driver cards. The program is then left running indefinitely to continuously measure the slurry. A month into the experiment, it was found that the computer had accumulated USB errors and stopped functioning. This is likely due to the large number of USB connections used. Internet connectivity was established and the peak-to-peak data was also uploaded though Dropbox each day. Remote access was established though LogMeIn in order to monitor computer and restart it if necessary.

#### 4.4.2 Initial Testing

After the sensor was constructed, some samples were provided for a lab test at the University of Alberta. The largest container available was a bucket capable of testing the 4 sensors 35 cm from the bottom; these are labeled B11a, B12, R13, and B13 from top to bottom.

The sample was labeled as Thickener Feed which had a solids content of 50%. The measurements were taken twice every half hour and continued on for 19 days. Interference between sensors B11a and B12 (10 cm apart) was minimised by measuring B11a with B13, and then measuring B12 with R13 (20 cm apart). The current for each laser diode was adjusted for a starting signal with the same voltage reading.

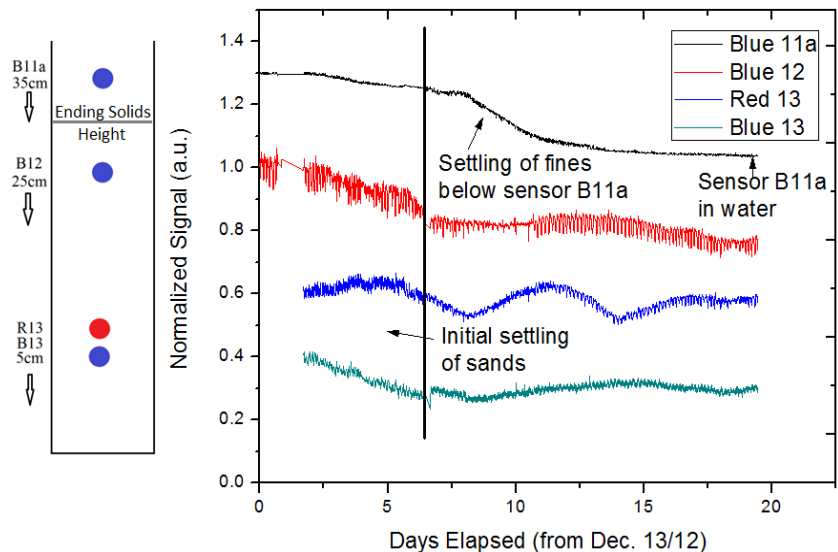


Figure 4-19 – Thickener Feed without flocculent. Schematic on the left shows the relative locations of the sensors and corresponds with the adjacent signals on the graph to the right. Colour available in electronic version.

Initially, all the signals decreased until approximately the 6<sup>th</sup> day of settling. This was interpreted as coarse sands settling out from the sample. When the experiment was finished, it was noticed that when attempting to stir the sample, there was a layer of about 1 or 2 cm of sand at the bottom of the bucket. After the 19 days of settling, the solids level was between sensors B11a and B12. Sensor B11a shows decrease in signal beginning around day 8 until it is entirely in clear water. The magnitude of the change in signal was relatively small compared to previous testing because of light reflection from the inside of the white bucket.

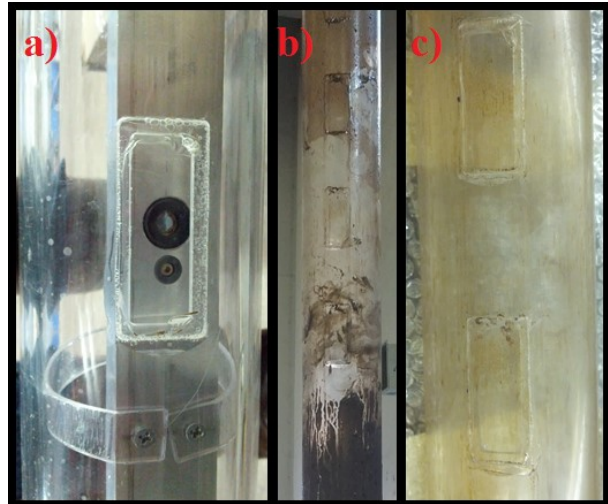


Figure 4-20 – Comparison of the window clarity a) before use, b) right after removal from the tank, and c) after rinsing with water

The window for B11a was clean once the solids level settled below it and there was no buildup of solids on the bottom ledge of the window. When the rod was removed from the sample, the tailings stuck to the tube because of its mud-like qualities, but they were easily rinsed off with a cup of tap water. Both these things suggest that the tailings should not stick strongly to the tube and block measurement.

#### 4.4.3 Results & Analysis:

After 1 year of measurement at the Saskatchewan Research Council facility, the sensor was removed. Figure 4-20 shows in b) the amount of solids stuck to the tube right after removal. The slurry had settled into a denser lower portion and an upper portion of murky water. The upper portion which is thinly coated in solids was in the ‘water’ portion and the

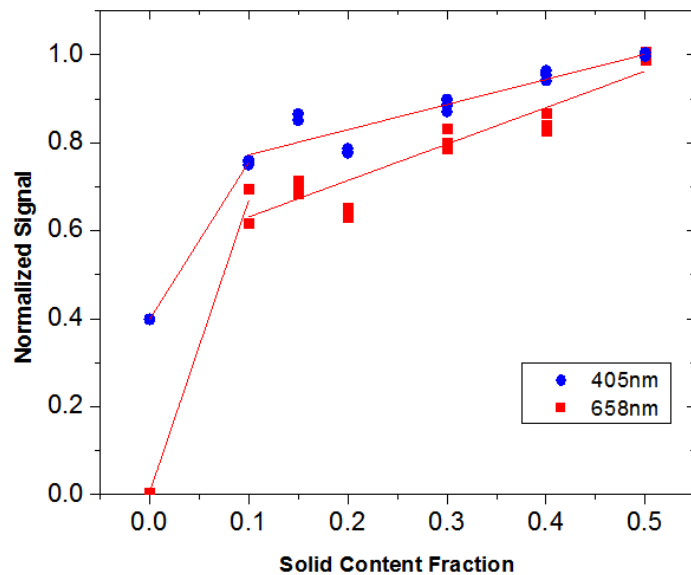


Figure 4-21 – Calibration curve for the MFT tested in the settling tank at 20° backscatter. The 0% for the blue laser is high because of small particulates which do not settle out. Colour available in electronic version.

lower part was in the solids. The middle section is where a hand had grasped the tube while removing it from the tank and it shows how easily the solids on the tube can be removed and a quick rinse with water washes away almost all of the solids sticking to the tube. It is likely that the coating is from the removal of the tube and it does not adhere and block the measurements. The rightmost picture shows that the tube underwent some yellowing which appears to be due to adsorption of hydrocarbons onto the plastic over time. On average, the light transmission of the windows was reduced to 65% and 80% when testing with the blue and red laser diodes respectively. Assuming that the surface was slowly coated over the experiment, the signal can be corrected based on the simple projection that the light passing through the window decreased linearly over the whole duration of the experiment. It is likely that the coating of the plastic may not be linear and that it reached a saturation point before the end of the experiment, but without further information a constant linear decrease can be used for approximation.

Before the start of the experiment, a sample of the slurry being tested was provided to use for calibration. The sample was diluted with deionized water and then measured using the calibration ring setup described previously. The maximum solids content fraction is 0.5 as provided. The light scatter signal decreases slowly with concentration at first, then rapidly as it approaches 'water'. It was observed that once the sample had been allowed to settle, the water layer on top was murky with some particles which would not settle; this was used for approximately 0% solids fraction sample. As can be seen in the calibration plot, red light had almost no scatter, but blue light was scattered back relatively strongly. An analysis program was developed to process the data from all the sensors and plot the calculated solids content fraction of each level over time based on this calibration.

Midway through the experiment at

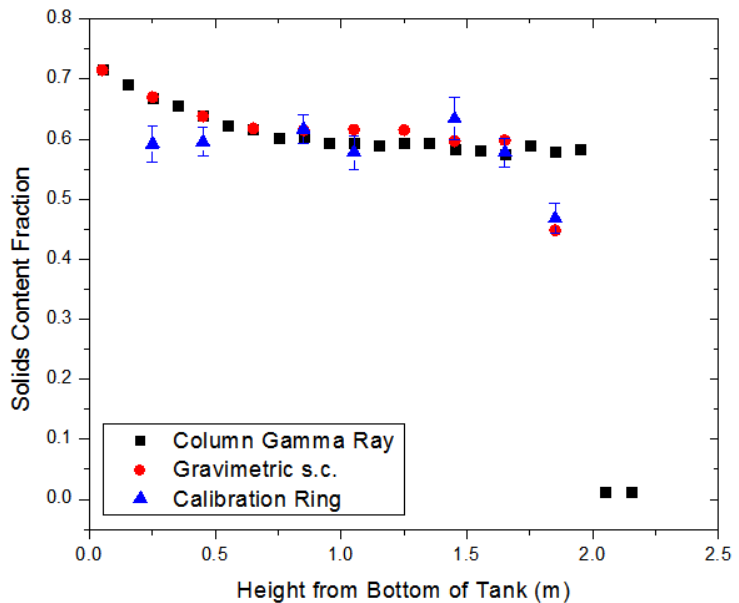


Figure 4-22 – Comparison of the gamma ray sensor and samples drawn from the tank, measured with gravimetric method (oven drying) and light scatter (calibration ring). The light scatter is signal fit to the gravimetric measurement. Colour available in electronic version.

the end of October 2013, samples were physically drawn from the tank for a direct measurement of the solids weight fraction. Some sample was also measured by light scatter using the calibration ring. This allows for comparison of facility's gamma ray sensor, gravimetric measurement of the samples by oven drying, the calibration ring's measurement of the drawn samples and the in-column light scatter measurements being taken. The gravimetric and gamma ray measurements agree very well as expected, except at 1.85 m from the bottom which is likely due to an error from sampling near the interface. The initial solids content fraction was 0.53. It shows that the solids content is very low where it looks like mostly water as expected, is somewhat constant at 0.6 in the middle of the tank, and near the bottom it increases up to 0.72. The calibration ring's measurements also follow this in general except for near the bottom of the tank where the signal does not increase and perhaps decreases slightly. It has been observed with sand samples that the light scatter signal increases up to 0.7, then decreases at 0.8 as discussed in the theory section. For less concentrated solutions, particles are surrounded by medium with lower index of refraction, which contributes to the scattered light. If the particles are packed very tightly, some of the light can pass from particle to particle which would reduce that reflected or scattered light because the change in index of refraction is minimal. In the limit where the solids are 100%, the light scatter will be very low, and dependent only on the surface roughness. This can be the cause for the decrease in signal for higher solid content.

The data from the sensors, for the blue laser diode, inside the settling tank follow the general trend of decreasing quickly at the upper levels but not as quickly for the lower levels. In Figure 4-23, levels 2 (L2) and 5 (L5, etc.) settle out much more quickly compared to levels 8 and 10 which are much lower in the tank. The solids content was calculated using the original calibration curve which does not take into account decreasing signals at higher solids content. Levels 8 and 10 continue to

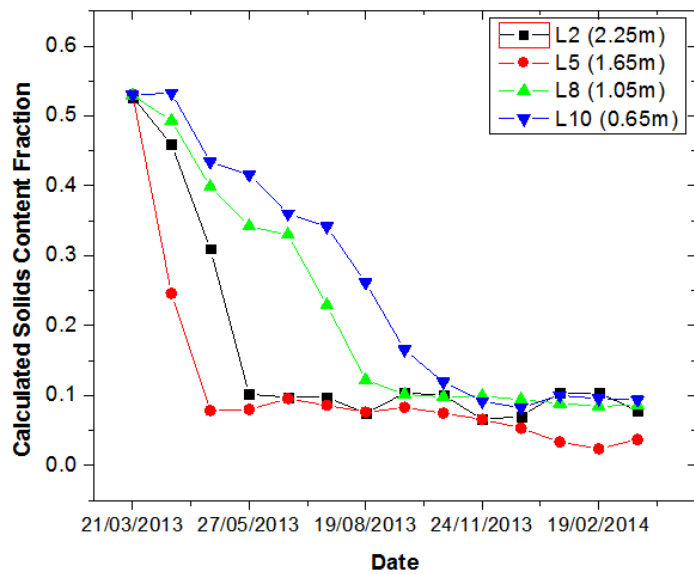


Figure 4-23 – Blue sensor data for 4 heights in the tank. The upper two sensors eventually reach ‘water’ whereas the lower two sensor remain in solids. Colour available in electronic version.

decrease until they are the same as the upper two levels, which is odd because the solids line does not settle past them. A possible cause of this is due to the plastic window being coated by bitumen and thus decreasing the transmission of light through it. This has a stronger effect over time as the window becomes more thickly coated, and as the signal decreases, the conversion assigns an even lower solids content value because of the steep region in the calibration curve.

There were some noise-like oscillations in the data which was especially prevalent with the signals for the red laser diode. It is unlikely that it is electronic noise for a few reasons. First, the same photodiodes, amplifier circuits, and data acquisition cards are shared between red and blue laser diodes at the same level; however, only 2 of the blue signals showed this kind of noise out of 7 red. Second, the length of an oscillation peak varies from level to level with no apparent pattern and is on the order of 5 to 15 days. This is much longer than is normally expected for electrical noise. It is also not likely caused by the laser diode because when the noise occurs for both red and blue signals at a level, the shape of the oscillations are very similar. The red and blue laser diodes on a particular level are controlled by different laser diode driver cards so it is unlikely that they would have the same shape of oscillation if the laser or laser driver was at fault. A possibility which could explain these oscillations are air bubbles trapped under the upper ledge of the window. When the sensor rod was removed, the tailings stuck to the tube like mud sticks to a boot. However, there were a few places where the upper part of the window was clear. These may have formed during the removal of the tube, but they may have also been trapped the whole time under a slight ledge of the window and unable to be released due to the viscous nature of the tailings. If these bubbles deform while the tailings settled around it, it could lead to unpredictable variations in the light scatter signal on the same timescale of 1 to 2 weeks. Additionally, the red laser diodes are positioned on the upper part of the window, which agrees with the fact that the red signals are the ones most often affected.



**Figure 4-24 – Clear section on the upper part of the window after the tube was removed. This is possibly caused by air bubbles, which may have affected measurements from the red laser diodes.**

#### **4.4.4 Summary**

The behaviour of the sensor follows the general expectation, however as noticed with the calibration ring measurements, the signal tends to decrease at high solids content. Further study into the light scatter signal from a settling sample as opposed to diluted samples should be performed for a better understanding on how to convert the signals to solid content data. Additionally, the signals are affected by particle size, which increases the complexity of analysis, but can provide valuable information about the sample.

There are a few design revisions which build on what was learned in this test experiment. To eliminate the necessity of windows, the sensor could be encased in a semi-circular tube with the flat pane serving as the window. The tube could then be made of other materials such as PVC which would simplify machining the tube and is available in a wider array of diameters and wall thicknesses. The material of the flat pane would be chosen to be glass or coated for oleophobicity to resist the slight collection of bitumen.

The electronics system can be made more efficient so that the controlling computer is not overloaded with USB devices. For example, two or more laser diodes could be connected in parallel to one channel on the FL 593 laser driver and controlled by a solid-state switch design. The NI-DAQ cards used for data acquisition are each equipped with 12 digital I/O which can control the switches. This could reduce the number of laser driver boards from 14 down to 1 – 3 boards. By multiplexing the detectors and laser diodes, all the sensors could be run with just one NI-DAQ. The laser diodes can also be chosen to have a built-in photodiode to enable constant power control to ascertain that the laser diode power output per current does not drift with time. LabVIEW is also overly complex for the needs of the sensor. The software needs to pulse the laser diode and possibly execute a feedback loop to control the laser diode power, and record data from the photodiodes. A much simpler programming language with less overhead can be used, such as a C based language.

## 4.5 Flow Sensor:

This sensor was to be used in a flowing pipeline in collaboration with a local start-up company Inline Dewatering. The company has developed a method for removing water from slurries and the sensor is positioned at the supply and return of the slurry storage tank as shown in the schematic. As

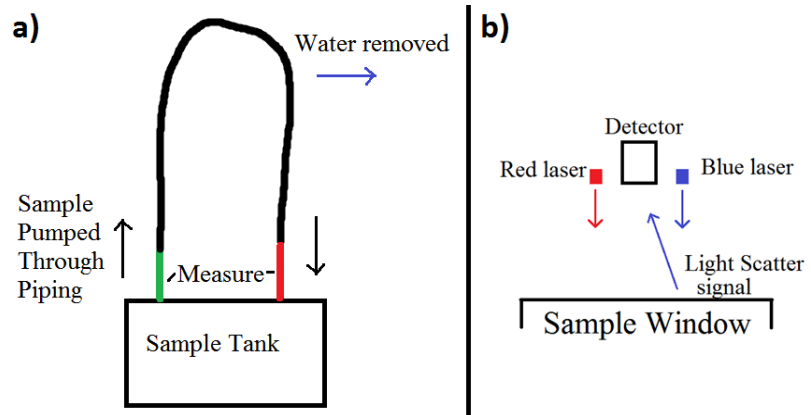


Figure 4-25 – (a) The sensors are placed at the supply and return of the sample tank. (b) The detector setup has two laser diodes flanking a photodiode detector above the sampling window. Light scatter is collected at a 20° angle.

the slurry is processed, the solids content at both the output and return can be monitored over time. The previous examples were typically measuring a decrease in solids content during settling, but this sensor is expected to measure an increase as the slurry is dewatered.

### 4.5.1 Design

#### *Housing*

The sensor was designed to be a section in the pipeline. A 1" diameter window was cut into the side of a 2" diameter PVC pipe. Initially the window was slightly recessed from the inner surface of the pipe because of concerns that the flowing slurry could scratch and degrade the clarity of the window. Unfortunately, the gap did not fill completely when slurry was passed through the pipe, causing an air bubble to be trapped and move around unpredictably on the surface of the window which affected the readings. Therefore a thicker window (17 mm thick) was cut from a block of polycarbonate which extruded slightly into the slurry flow. To the date of this writing, the window clarity has not degraded noticeably.

Around the window another short section of pipe was glued perpendicular to main pipe and a cap holding the laser- and photodiodes would be screwed on top to block out ambient light. The sensor consisted of a blue (405 nm) and red (639 nm) laser diode along with a photodiode. The controlling device was a Raspberry Pi (RPI), which is a credit card-sized microprocessor using a Linux operating system and uses USB power, like a phone charger. It was originally connected to the Wi-Fi network

with a USB dongle, but due to poor connectivity, the on-board Ethernet port was used instead. The RPi can be connected to a keyboard, mouse and monitor to behave like a desktop computer and this was how development with it was carried out. It can also be connected to the internet and remotely accessed. It comes ready with a graphical operating system, but the text-based system was used for simplicity.

### ***Sensory Systems***

The same photodiode was used for detection. The RPi has 5 V and 3.3 V supplies in its General Purpose Input/Output (GPIO) and a goal was to utilise this as the power supply. The GPIO supports only digital inputs and outputs so an analog to digital converter (ADC) chip was used and communicated initially with software control or ‘bit banging’ but later updates allowed for Serial Peripheral Interface (SPI) hardware control to be used for faster performance. The ADC is an MCP3008 8 channel, 10 bit converter and it was setup to use the 3.3 V as a reference. This was done because the RPi 5 V supply depends on the USB wall adapter which is specified to  $5 \pm 0.25$  V. The 5 V will droop with a load depending on the manufacturer of the adapter and the minimum voltage measured with the current adapter is 4.78 V. The 3.3 V is supplied from a linear regulator and is effectively constant, regardless of input voltage, for this purpose. Using the 3.3 V as a reference for the ADC also gives higher resolution (3 mV step). The op-amp used was an MCP6004 which allows for a single supply rail of 5 V. To accommodate this, the photodiode was connected in reverse

(anode grounded) to provide a positive voltage signal. Since the photodiode used an SMA connector (SubMiniature version A) this caused slightly higher than normal noise in the signal as the coaxial cable was used in reverse. In the future, an anode grounded photodiode will be used. A similar amplification stage was used with 30 mV/nA gain, followed by 2 simple second order low-pass Sallen-

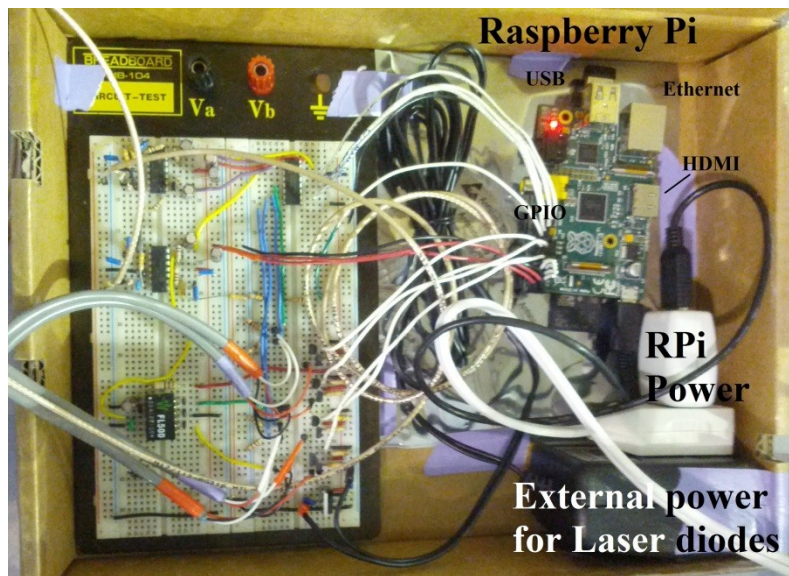


Figure 4-26 – Flow sensor electronics. Raspberry Pi and power supply at right and at left breadboard circuitry for amplifying, sending, and reading signals.

Key filters with a corner frequency of 10 Hz which were used to filter noise.

The laser diodes are 5.6 mm diameter 405 nm and 639 nm wavelength with a max output of 20 mW and 10 mW respectively. They are equipped with photodiode feedback which will be used and is explained in the next section. The laser diodes are housed in a small holder with an adjustable lens for collimation. The spacing between the laser and photodiodes was made to observe the 20° scatter, taking into account the thicker window.

### ***Electronics & Software***

The laser driver circuit utilised just the FL500 chip as opposed to the FL593 laser driver board for simplicity of operation. Since the RPi GPIO does not have analog output, a pulse width modulated (PWM) signal was used at 125 Hz which is fast enough not to affect the load. The PWM duty cycle has a granularity of 10  $\mu$ s, so lower frequencies or higher periods allow for finer tuning of the laser output power. The PWM signal was passed through the same design of 2 second order low-pass filters to average it into an analog signal because the FL500 is specified to be responsive up to a 100 kHz square wave. The voltage signal is used by the IC to control the laser diode current and its magnitude is controlled simply by changing the duty cycle % of the PWM signal and has granularity of 0.125%. The laser diodes used have built-in feedback photodiodes which are reverse biased because of the laser diode package's 3-pin configuration and the photocurrent is converted into a voltage via a 2 k $\Omega$  resistor which is directly read by the ADC chip. The red diodes (Style A) and blue diodes (Style B) have slightly different configurations as can be seen in the circuit diagram schematic located in the appendix. Both are connected together in parallel to an input of the FL500 laser driver but the on/off state of each laser diode is controlled by a pair of MOSFETs and only one diode is on at a given moment. The 5 V supply from the RPi was not able to adequately power the blue laser diodes which have a forward voltage drop of 5 V to 6.5 V. A simple boost converter was implemented to increase the voltage available, but the current draw was too high with the available 0.5 A supply USB adapter and the RPi power input is fused at 0.75 A. An external 12 V DC wall adapter was regulated at 8 V with a linear regulator and used to supply the power instead. In future revisions, the external supply can also be regulated at 5 V to supply the RPi.

The circuitry for this device was built on a breadboard for testing and easy modification. A schematic of it has been made in Eagle CAD for organization. This can sent out to be manufactured into a PCB in the future. The PCB would plug into the RPi's GPIO pins and sit directly above the RPi reducing its footprint greatly. PCBs also create much more robust connections which are soldered together and

do not suffer from wires being dislodged when they are stressed. Connections which go off-board can use a screw terminal. Lastly, noise is expected to be decreased due to printed traces instead of long wires and generally better connections. The electronics housed in the box were placed in a splash-proof plastic box to ward against water and slurry sprays which are not an uncommon occurrence.

The software was written using Python. Since the laser diodes used in this project had a built-in feedback photodiode, a proportional-integral (PI) algorithm was implemented from scratch to control the laser current to achieve a laser power setpoint. This was made to run in parallel using Python's 'threading' module to maintain the laser diode power at a setpoint anytime the laser diode was turned on. With the constant power control, no warm-up time was necessary and measurements were taken immediately. For each measurement, the raw data was saved, and the peak-to-peak of the signal was calculated. The duty cycle of the PWM signal and the laser diode feedback photodiode current were also logged for each measurement. The RPi does not have a real-time clock or battery like a laptop, but with internet connectivity it keeps itself synchronized with UTC time and this was used to time stamp measurements. A 4 GB SD card acts as the RPi's hard drive and is where the data is saved locally. The data can then be received by accessing it remotely through the local network, or, if necessary, directly through a USB drive. For each experiment, the RPi would be controlled through remote access over the local network to start or stop it, and take the data.

The reason behind using the RPi is to simplify the sensor setup. LabVIEW has a vast amount of capability, but most of its features are not used here and the bulk of the laptop's operating system and supplemental software can cause unnecessary software complications. Alternatively a microcontroller could be used such as a PIC Microcontroller, where many can be easily implemented in parallel; however, it brings more complexity with user interfacing (i.e. to extract the data and change settings). The RPi is a compromise between the two having a simple and clean environment and a reasonable interface. Currently the command line mode of the Linux operating system is used to run the Python software; a GUI can be made relatively easily from the built-in PyGame package since instrument panels and video game controls share much in common. If this is to be applied to the insertion sensor or where a large number of laser diodes and photodiodes are required, a multiplexing scheme was briefly investigated and can be used to reduce the number of I/O ports and additional chips or devices required. In conjunction with, or as an alternative to multiplexing, the RPi

can communicate using Universal Asynchronous Receiver/Transmitter (UART) with microcontrollers such as the PIC. Many PICs can be setup in a network, each with a small number of sensors, to handle data collection and processing, while the RPi handles the user interface and exporting data. This would allow easy scaling to large numbers of sensors.

#### 4.5.2 Results

Data was collected during slurry processing test and were compared against sample density measurements. On-site personnel took density measurements by sampling from the slurry/sample tank and measuring the weight and volume. This can be converted to solids content ranging from 30% to 45%.

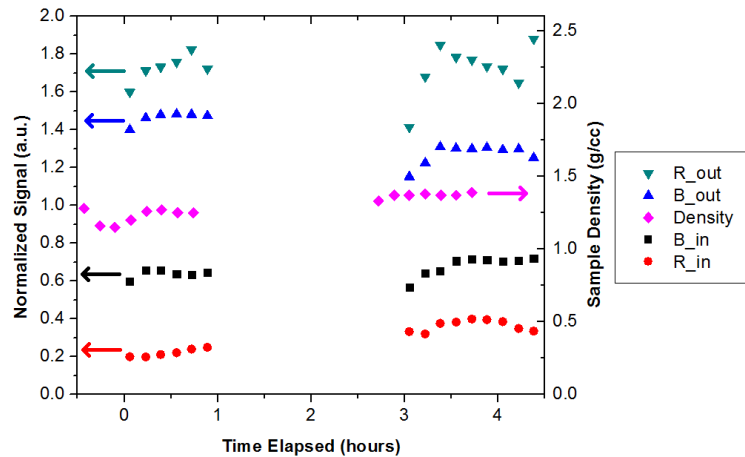


**Figure 4-27 – A comparison of data between light scatter measurements and the sample’s density. Normalized light scatter signal (measured at 20°) shown above and below the measured density of the slurry.**

Two measurements were taken at the input and output of the slurry storage tank as described above and are named with respect to the wavelength of light used – red (R) or blue (B) – and its location – in or out. As usual, the scattering was observed at a 20° angle. The time scale in Figure 4-27 starts when the RPi measurements began, which happened slightly after the sample density measurements occurred. In principle, the calibration obtained in Section 4.2 can be used to convert the light scatter signal to solids content. In this case, the signal varies much more compared to the calibration data shown in Figure 4-12 and would lead to the solids content changing wildly above 100%. More understanding of how the light scatter signal behaves between different setups is needed before the data here can be directly compared with the sample density. Looking at the data, the light scatter signal, especially the blue, appears to vary in relation to the changes in sample density. This is most apparent in the first experiment. The testing was then stopped, and restarted after 2 hours where some parameters of the slurry processing were changed. At this point the signals on the output side decreased a relatively large amount compared to the sample density. This signifies a decrease in light detected by the photodiode because the laser diodes are operated with a fixed output power. This could be

due to condensation forming on the sensory optics as discussed below. It was also noted that the output side sensor tends to build up condensation much more quickly compared to the input side.

During some measurements, it was noticed that condensation was building up on both the photodiode and laser diode lenses. The slurry heats up to approximately 60°C during processing and the ambient temperature was around 10°C in the warehouse where the experiment was set up which noticeably interfered with a number of experiments. For the data shown in Figure 4-27, the ambient temperature was about 20°C. A few approaches could be taken to stop the condensation: heating near the laser and photodiodes to bring the temperatures closer together should reduce condensation. Desiccant could be used to absorb excess moisture in the sensor housing. Finally, dry air could also be flowed through the sensor housing.

### **4.5.3 Summary**

The improved design of the sensory system worked very well, although continuous long-term testing on the scale of many months was not carried out. When the RPi was wired directly to the network, the sensor functioned well and did not experience crashing or freezing. It was also able to be easily operated by personnel at the testing site, which is important for a useful sensor system. The constant power operation of laser diode implemented here help to ascertain the stability of the laser diode operation, which is important in determining light scatter signal measurements. Testing is ongoing, but the initial results of the sensor show that the light scatter signal changes in response to the sample density changes, but a better understanding of how to directly convert the light scatter signal to solids content will be developed in the future. Finally, the window design was successful and did not show any obvious signs of degradation which allows live measurement of slurry flowing through a pipeline.

## 5. Summary & Future Directions

Two sensors were developed in this work: a compact fluorescence spectrometer and a light scatter sensor for slurry solids content analysis. These two devices were developed with an emphasis on a cost-effective, portable system to provide on-location results for rapid decision making.

First, a fluorescence spectrometer was developed for the detection of hydrocarbon contaminants in soil and was made to be compatible with CPT, which restricted the dimensions to a 25 mm diameter tube. Five long-pass filters with successive cut-off wavelengths were used to divide the spectrum into four sections, which were then used to distinguish various samples, including multi-ringed aromatic hydrocarbons, typical constituents of MFT and crude oil. Resolution is the typical metric for a spectrometer and the purpose is to analyse the details of the spectrum. In this case, the emphasis is on portable, compact packaging with resolution that is sufficient to distinguish between compounds of interest. The sensor was capable of distinguishing between green paper and pyrene, which has a 28 nm difference in peak wavelength. This was due to the peaks proximity to a filter cut-off wavelength, where the resolution is higher for the device. Using this method, the filter cut-offs can be designed for maximum sensitivity in the wavelength ranges of interest. Furthermore, only 5 filters, 7 mm in diameter, were used for this prototype. More filters can easily fit in the sensor, or other methods such as linear variable filters or transmission gratings can be investigated. This device uses a single 405 nm laser diode as the excitation source; however use of multiple sources with different wavelengths can be developed to build an EEM which improve its ability to distinguish between compounds. Finally, this prototype was developed with the space constraints in mind, but also for ease of testing in the lab environment, so some changes are required to realize a device which is completely compatible with CPT. A design was discussed which addresses these issues and suggests possibilities for developing this field-test design.

The second part of this work is the development of light scatter sensors for measuring the solids content or concentration of a slurry. Light scatter is a typical method of measuring particle size and concentration, but only for very dilute samples where the single scatterer approximation applies, compared to 30% to 70% w/w concentrations encountered with slurries. Light scatter was empirically studied and found to have 3 regions of response. At low concentrations, the light scatter signal increases rapidly with increasing solids content. At medium concentrations, the relative increase in solids content slows down, but continues to increase with solids content. Finally, at very high solids content, the light scatter begins to decrease with increasing solids content. The main

application investigated here was to measure the change in solids content for settling oil sands tailings. First a device was developed to monitor the progress of tailings settling due to gravity, but there are many methods which industry uses to accelerate the rate of settling. A device was developed to withstand 100 times gravity for use in centrifuging method. Another was for large scale and long term settling using flocculent. Finally, a sensor was developed for use on a flowing pipeline, measuring the solids content change as the slurry was processed to remove water. These tests of initial devices show responsiveness of the light scatter signal to the changing solids content. Some improvements to the hardware and software designs learned from field testing are discussed in the respective sections. LabVIEW is good for executing complex programs, but along with the operating system used and additional background services, does not allow for continuous operation of the sensor without intervention because of small error which accumulates over time. Additionally, the software required to run the sensor does not need to use all the capabilities of LabVIEW. The Raspberry Pi used in the next sensor runs minimalistic version of Linux and the software is executed in Python. The software written to run the sensor is relatively very simple and is expected to be more successful at continuous operation over long amounts of time. The drawback here is that the RPi has much less computing compared to a laptop. This could be offset by using the RPi to communicate with microcontrollers and offload some of the more computationally intensive tasks such as executing the feedback control for the laser diode output power. The focus of further development will be in simulating and understanding for light scatter of highly concentrated particles of various size distributions and for irregular shapes.

## 6. Bibliography

- [1] BGC Engineering Inc., "Oil Sands Tailings Technology Review," Oil Sands Research and Information Network, University of Alberta, School of Energy and the Environment, Edmonton, Alberta, 2010.
- [2] M. Gupta, Y. Zhou, T. T. Ho, A. Sorta, M. T. Taschuk, D. C. Segó and Y. Y. Tsui, "Solid Content of Oil Sands Tailings Measured Optically," in *Third International Oil Sands Tailings Conference*, Edmonton, Alberta, 2012.
- [3] T. T. Ho, M. Gupta, M. T. Taschuk, M. Alostaz, A. Ulrich, D. C. Segó, R. Dolling, D. Woeller and Y. Y. Tsui, "Fluorescence Spectrophotometer for Cone-Penetrometer Applications," in *Third International Oil Sands Tailings Conference*, Edmonton, Alberta, 2012.
- [4] M. Taschuk, Q. Wang, S. Drake, A. Ewanchuk, M. Gupta, M. Alostaz, A. Ulrich, D. Segó and Y. Y. Tsui, "Portable Naphthenic Acid Sensor for Oil Sands Applications," in *Second International Oil Sands Tailings Conference*, Edmonton, Alberta, 2010.
- [5] E. W. Allen, "Process water treatment in Canada's oil sands industry: I. Target pollutants and treatment objectives," *Journal of Environmental Science*, vol. 7, pp. 123-138, 2008.
- [6] E. Slavcheva, B. Shone and A. Turnbull, "Review of naphthenic acid corrosion in oil refining," *British Corrosion Journal*, vol. 34, pp. 125-131, 1999.
- [7] ConeTec Investigations Ltd. & ConeTec Inc., "UVIF Cone Penetration Testing," ConeTec, 2010. [Online]. Available: [www.conetec.com](http://www.conetec.com). [Accessed April 2014].
- [8] Malvern Instruments Ltd, "Dynamic light scattering for particle size characterization," Malvern Instruments Ltd, 2014. [Online]. Available: [www.malvern.com](http://www.malvern.com). [Accessed April 2014].
- [9] LS Instruments , "LS Instruments AG," LS Instruments, 2014. [Online]. Available: [www.lsinstruments.ch/](http://www.lsinstruments.ch/). [Accessed April 2014].

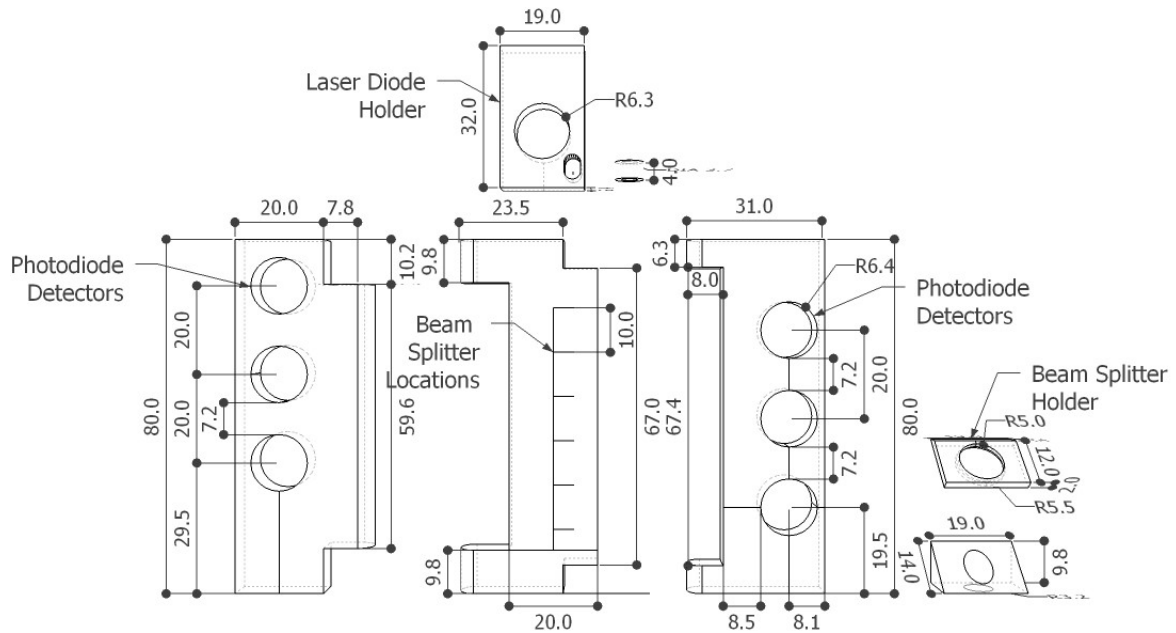
- [10] E. Hecht, Optics 4th Edition, San Francisco, CA: Pearson Education, Inc., 2002.
- [11] J. R. Lakowicz, Principles of Fluorescence Spectroscopy 3rd Edition, New York, NY: Springer Science+Business Media, 2006.
- [12] N.J.Turro, V. Ramamurthy, W. Cherry and W. Farneth, "The Effect of Wavelength on Organic Photoreactions in Solution. Reactions from Upper Excited States," *Chemical Reviews*, vol. 78, no. 2, pp. 125-145, 1978.
- [13] M. Alostaz, K. Biggar, R. Donahue and G. Hall, "Petroleum contamination characterization and quantification using fluorescence emission-excitation matrices (EEMs) and parallel factor analysis (PARAFAC)," *Journal of Environmental Engineering and Science*, vol. 7, pp. 183-197, 2008.
- [14] L. D. Brown, M. Alostaz and A. C. Ulrich, "Characterization of Oil Sands Naphthenic Acids in Oil Sands Process-Affected Waters Using Fluorescence Technology," in *Geo Halifax 2009*, Halifax, NS, 2009.
- [15] H. van de Hulst, Light Scattering by Small Particles, Toronto, ON: General Publishing Company Ltd., 1981.
- [16] C. F. Bohren and D. R. Huffman, Absorption and scattering of light by small particles, New York: Wiley, 1998.
- [17] P. Laven, "Simulation of rainbows, coronas, and glories by use of Mie theory," *Applied Optics*, vol. 42, no. 3, pp. 436-444, 2003.
- [18] Point Grey Research Inc., "Technical Reference Manual," 12 July 2011. [Online]. Available: <http://ww2.ptgrey.com/USB2/chameleon>. [Accessed 27 December 2013].
- [19] I. B. Berlman, Handbook of fluorescence spectra of aromatic molecules 2nd Edition, New York, NY: Academic Press Inc., 1971.
- [20] HEICO Engineering Services Pvt. Ltd. , "Hydraulic and Engineering Instruments," HEICO Engineering Services Pvt. Ltd., 2010. [Online]. Available: <http://www.heico.in.com/index.php>.

[Accessed April 2014].

[21] I. Polysciences, "Polysciences, Inc.," Polysciences, Inc., 2014. [Online]. Available: <http://www.polysciences.com/>. [Accessed April 2014].

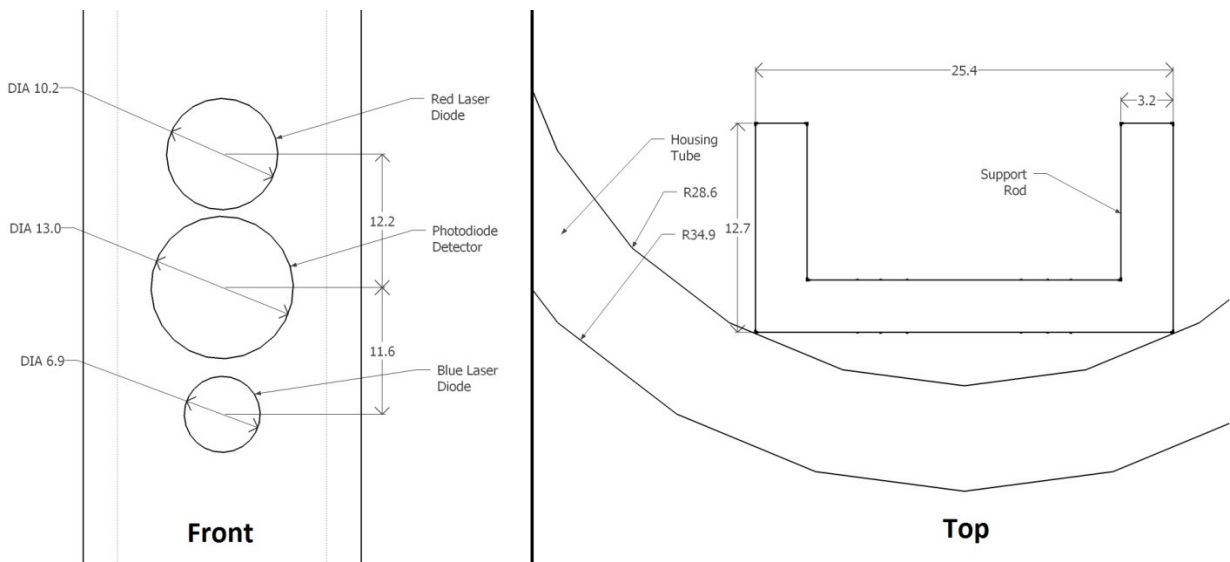
# Appendix A: Schematics for Devices

## Centrifuge Sensor



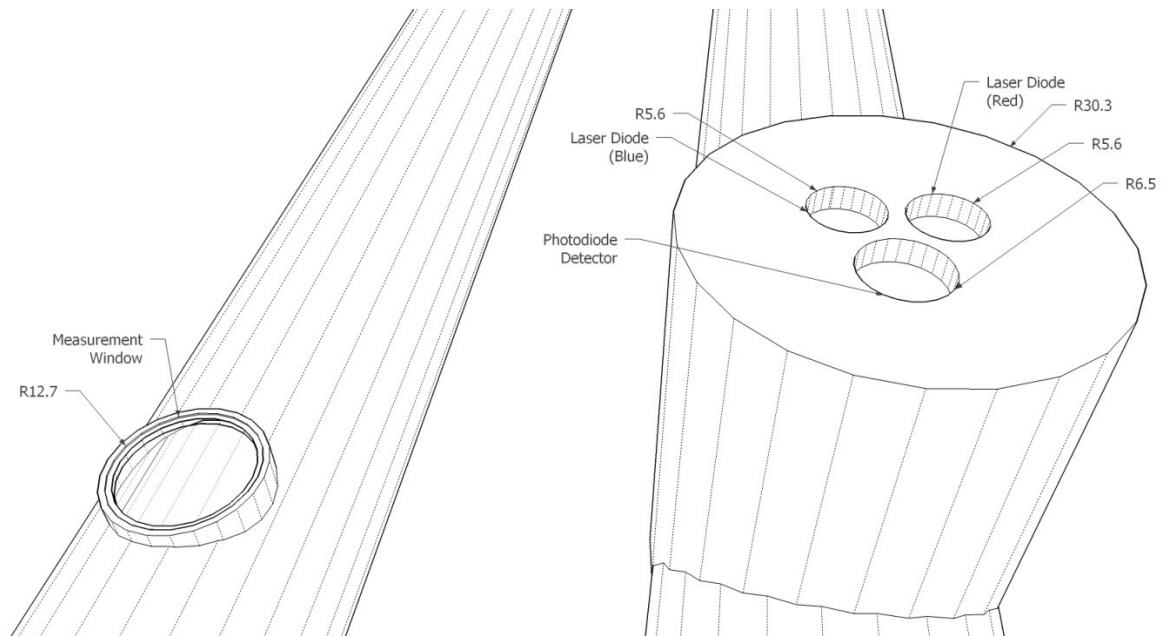
This is the schematic of the centrifuge sensor (1 cm spacing) with dimensions and it made from aluminum. The dimensions are in millimetres.

## Insertion Sensor



The front shows the positioning of the photo- and laser diodes, and the top shows how it fits into the clear housing tube. The dimensions are in millimetres.

## Flow Sensor



On the left, the window is shown cut into the side of the pipe. The right shows how cap fits above the window, with the photo- and laser diodes. The dimensions are in millimetres.

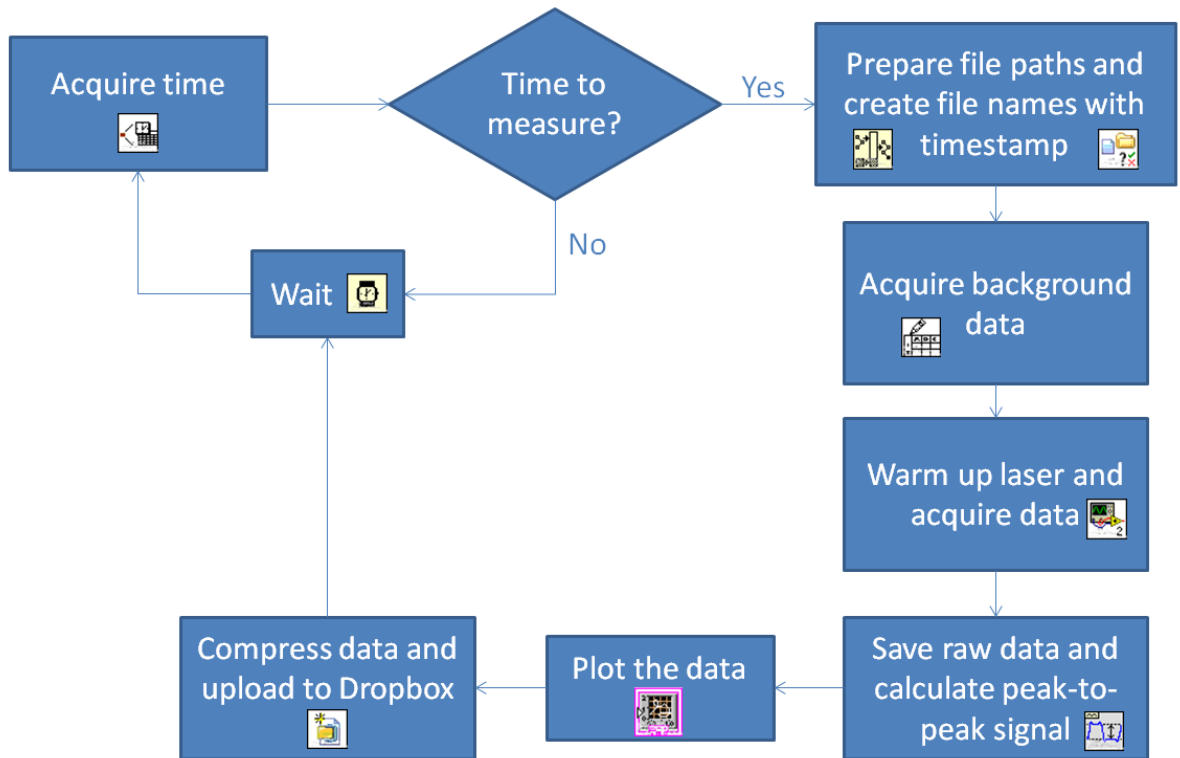


The upper left of the diagram shows the various connections made with the RPi. It supplies +3 V and +5 V required for the rest of the circuitry. The pins used are to toggle the enable of the laser diode, to supply the PWM signal for controlling the laser diode output power, and the SPI communication with the analog/digital converter chip. The upper center shows the +8 V regulator which supplies power to the laser diodes from an external 12 V AC-DC adapter. The upper right of the diagram contains the control for the laser diodes. Each pair of laser diodes (one red and one blue) are connected to one channel of the FL500 laser driver, but they are enabled individually by a pair of MOSFET switches, which are default off. The center left of the schematic shows the two low pass filters used to convert the PWM signal into an analog signal, since the FL500 chip is capable of up to 100 kHz square wave operation. The lower part of the schematic, starting from the left, shows the transimpedance amplifier used to convert the photocurrent to a voltage signal (30 mV/nA) and then passed through two low pass filters to remove noise. The lower right shows the analog to digital conversion chip. Channels 0 and 1 are for the photodiode signal, channel 3 is used to monitor the setpoint voltage used to control the laser diode output power, and channels 4 to 7 monitor the photodiode feedback of the laser diodes and are used in achieving constant power control.

## Appendix C: Software

### Insertion Sensor

LabVIEW is a block diagram programming language. This flowchart outlines the operation of the code.



### Flow Sensor

The software for the flow sensor is written for Python and is very similar to the above LabVIEW code. The code is commented to explain the function of each section.

```
001 import time
002 import threading
003 import RPIO
004 import io
005 import spidev
006 import os
007 from RPIO import PWM
008 from time import strftime
009
010 # Check for existance of directory
011 def check_dir(f):
012     d = os.path.dirname(f)
013     if not os.path.exists(d):
014         os.makedirs(d)
015
016 # Read from SPI pins; MCP3008
017 def readadc(adcnum):
```

```

018     if ((adcnum>7) or (adcnum<0)):
019         return -1
020     # input format is array:
021     # start bit(S), single/double ended bit(E), 3 channel # bits (CCC), don't care (X)
022     #         0b [0000 000S, ECCC XXXX, XXXX XXXX]
023     # output is 0b [XXXX XXXX, XXXX XX00, 0000 0000] where 0 is data
024     # output format is list of bytes 0xAB 0xCD 0xDE
025
026     result = spi.xfer2([0x01, (adcnum | 8) << 4, 0x00]) #xfer2 keeps CE asserted for
whole transmission
027     adcout = ((result[1] & 3) << 8) | result[2] # remove unwanted front 6 bits and append
028     return adcout
029
030 # Add the PWM pulses on demand
031 class PWMPulse:
032     def __init__(self, channel, gpio, cyc, gran):
033         PWM.init_channel(channel, cyc)
034         self.channel = channel # PWM channel
035         self.gpio = gpio # GPIO pin
036         self.gran = gran # pulse granularity
037         self.cyc = cyc # period of pulse
038         self.width = 0 # pulse width
039         if not PWM.is_channel_initialized(channel):
040             PWM.init_channel(channel, cyc)
041     def pulse(self, dc):
042         self.width = min(int(dc / 100.0 * self.cyc / self.gran), int(self.cyc/self.gran)-
1)
043         self.width = max(self.width, 0)
044         PWM.add_channel_pulse(self.channel, self.gpio, 0, self.width)
045     def stop(self):
046         PWM.clear_channel(self.channel)
047
048 # PID controller based off of Wikipedia: http://en.wikipedia.org/wiki/PID controller
049 class PID:
050     def __init__(self, Kp, Ki, Kd, setpoint):
051         self.Kp = Kp
052         self.Ki = Ki
053         self.Kd = Kd
054
055         self.error = 0.0
056         self.lasterr = 0.0
057         self.setpoint = setpoint
058
059         self.integral = 0.0
060         # u = P + I + D variable holders
061         self.P = 0.0
062         self.I = 0.0
063         self.D = 0.0
064         self.u = 0.0
065     def update(self, current):
066         self.error = self.setpoint - current
067         # Calculate P part
068         self.P = self.Kp * self.error
069         # Calculate I part
070         self.integral += self.error # No need to worry about overflow in Python
071         self.I = self.Ki * self.integral
072         # Calculate D part
073         self.D = self.Kd * (self.error - self.lasterr)
074         self.lasterr = self.error
075         # Sum them together
076         self.u = self.P + self.I + self.D
077         return self.u
078     def set(self, setpoint):
079         self.setpoint = setpoint
080
081 # Maintain constant power based on LDPD readout
082 # Calling PID to calculate next value and PWMPulse to set output
083 class constPower(threading.Thread):
084     def __init__(self, LDPDchannel, LD_pin, lasermax):
085         threading.Thread.__init__(self)
086         self.quit = False # only called when time to stop

```

```

087     self.channelRin = LDPDchannel[0]    # Rin - Channel of the LD's PD on ADC
088     self.channelBin = LDPDchannel[1]    # Bin
089     self.channelRout = LDPDchannel[2]   # Rout
090     self.channelBout = LDPDchannel[3]   # Bout
091     self.lasemax_r = lasemax[0]        # Red laser maximum duty cycle
092     self.lasemax_b = lasemax[1]        # Blue laser maximum duty cycle
093     self.LD_pinRin = LD_pin[0]         # GPIO pin to turn on LDs
094     self.LD_pinBin = LD_pin[1]
095     self.LD_pinRout = LD_pin[2]
096     self.LD_pinBout = LD_pin[3]
097     self.LDPDsig = 0.0                  # Temp storage for LDPD signal
098     self.PIDdc = [0.0, 0.0, 0.0, 0.0]  # Current duty cycle of LD
099     def run(self):
100         while not self.quit:
101             ## RED INPUT SIDE ##
102             if RPIO.input(self.LD_pinRin): # If (which) laser diode is on, update pid
103                 with ADClock:
104                     self.LDPDsig = readadc(self.channelRin)
105                     self.LDPDsig *= 3300.0 / 1023.0 / 2 # = LDPDsig / 1023 bins * 3300mV ref
/ 2kOhm resistor => uA
106                     self.PIDdc[0] = pidList[0].update(self.LDPDsig)
107                     # do not overstep laser extrema
108                     if self.PIDdc[0] > self.lasemax_r:
109                         self.PIDdc[0] = self.lasemax_r
110                     # Write output to PWM
111                     p.pulse(self.PIDdc[0])
112             ## BLUE INPUT SIDE ##
113             elif RPIO.input(self.LD_pinBin):
114                 with ADClock:
115                     self.LDPDsig = readadc(self.channelBin)
116                     self.LDPDsig *= 3300.0 / 1023.0 / 2 # = LDPDsig / 1023 bins * 3300mV ref
/ 2kOhm resistor => uA
117                     self.PIDdc[1] = pidList[1].update(self.LDPDsig)
118                     # do not overstep laser extrema
119                     if self.PIDdc[1] > self.lasemax_b:
120                         self.PIDdc[1] = self.lasemax_b
121                     # Write output to PWM
122                     p.pulse(self.PIDdc[1])
123             ## RED OUTPUT SIDE ##
124             elif RPIO.input(self.LD_pinRout):
125                 with ADClock:
126                     self.LDPDsig = readadc(self.channelRout)
127                     self.LDPDsig *= 3300.0 / 1023.0 / 2 # = LDPDsig / 1023 bins * 3300mV ref /
2kOhm resistor => uA
128                     self.PIDdc[2] = pidList[2].update(self.LDPDsig)
129                     # do not overstep laser extrema
130                     if self.PIDdc[2] > self.lasemax_r:
131                         self.PIDdc[2] = self.lasemax_r
132                     # Write output to PWM
133                     p.pulse(self.PIDdc[2])
134             ## BLUE OUTPUT SIDE ##
135             elif RPIO.input(self.LD_pinBout):
136                 with ADClock:
137                     self.LDPDsig = readadc(self.channelBout)
138                     self.LDPDsig *= 3300.0 / 1023.0 / 2 # = LDPDsig / 1023 bins * 3300mV ref
/ 2kOhm resistor => uA
139                     self.PIDdc[3] = pidList[3].update(self.LDPDsig)
140                     # do not overstep laser extrema
141                     if self.PIDdc[3] > self.lasemax_b:
142                         self.PIDdc[3] = self.lasemax_b
143                     # Write output to PWM
144                     p.pulse(self.PIDdc[3])
145                     time.sleep(0.005)
146                     #print(time.clock() - self.testtime)
147         def stop(self):
148             self.quit = True    # time to stop
149
150     # SETUP:
151     # SPI pins are hardwired
152     # Using BCM pin no.
153     ## Laser on/off pin ##

```

```

154 LD_pin = [17, 18, 22, 23] # [Rin, Bin, Rout, Bout]
155 ## PWM Variables ##
156 PWM_pin = 24 # PWM output affects all lasers. Laser on/off state is determined by
LD_pin
157 CYC_PERIOD = 8000 # in us, 4000 is minimum
158 GRAN = 10 # pulse width increment granularity
159 PWM_addr = 0 # use PWM DMA channel 0
160
161 time_str = strftime("%Y_%m_%d_%H_%M_%S")
162 day_str = strftime("%Y_%m_%d")
163 file_name = ['_Rin.txt', '_Bin.txt', '_Rout.txt', '_Bout.txt']
164 file_loc = '/home/pi/sensor/data/'+day_str+'/'
165 file_net = '/home/pi/NetDrive/RaspiPi/SensorData/'+day_str+'/'
166 check_dir(file_loc)
167 check_dir(file_net)
168 num_pulses = 20 # Number of pulses with which to average signal over
169
170 ## PID control variables ##
171 lasermax = [80.0, 100.0] # maximum output of laser, in duty cycle
172 power = [180, 170, 120, 150] # setpoint in uA [red, blue]
173 ## PID control gains ##
174 Kp = [0.00600, 0.00100, 0.00600, 0.00100] # Proportional gain
175 Ki = [0.00060, 0.00090, 0.00060, 0.00090] # Integral gain
176 Kd = [0, 0, 0, 0] # Don't use Differential gain
177
178 ## Data acquisition ##
179 ADClock = threading.Lock()
180 spi = spidev.SpiDev()
181 spi.open(0,0) # Bus 0, CS 0
182 # Channel no. of ADC input
183 LDPD_chan = [7, 6, 5, 4] # Laser diode's PD, for constant power
184 PWM_chan = 2 # Monitor the PWM output DC voltage
185 PD_chan = [0, 1] # PD on the [input, output] side
186
187 RPIO.setup(LD_pin[0], RPIO.OUT, initial=RPIO.LOW) # on/off toggle
188 RPIO.setup(LD_pin[1], RPIO.OUT, initial=RPIO.LOW)
189 RPIO.setup(LD_pin[2], RPIO.OUT, initial=RPIO.LOW)
190 RPIO.setup(LD_pin[3], RPIO.OUT, initial=RPIO.LOW)
191 PWM.setup() # PWM output
192 PWM.set_loglevel(PWM.LOG_LEVEL_ERRORS)
193
194 p = PWMPulse(PWM_addr, PWM_pin, CYC_PERIOD, GRAN) # PWM output
195 pidRin = PID(Kp[0], Ki[0], Kd[0], power[0]) # P I D setpoint
196 pidBin = PID(Kp[1], Ki[1], Kd[1], power[1]) # P I D setpoint
197 pidRout = PID(Kp[2], Ki[2], Kd[2], power[2]) # P I D setpoint
198 pidBout = PID(Kp[3], Ki[3], Kd[3], power[3]) # P I D setpoint
199 pidList = [pidRin, pidBin, pidRout, pidBout]
200 constP = constPower(LDPD_chan, LD_pin, lasermax)
201 p_to_p= [0.0, 0.0, 0.0, 0.0]
202
203 constP.start()
204 # LD/PID warmup, get PID settings started
205 time_start = time.time()
206 for warm in range(4):
207     RPIO.output(LD_pin[warm], 1)
208     print("Warming up...")
209     time.sleep(2)
210     RPIO.output(LD_pin[warm], 0)
211     print("Done.")
212 # Prepare output text files
213 # with open((file_loc+file_name[warm]),'w') as ftxt:
214 #     ftxt.write("Time(h)\tDC(%) \tPD(mV) \tLDPDsig(mV)\r\n")
215 # with open((file_net+file_name[warm]),'w') as ftxt:
216 #     ftxt.write("Time(d)\tDC(%) \tPD(mV) \tLDPDsig(mV)\r\n")
217 with open((file_loc+'Peak2peak.txt'), 'w') as ftxt:
218     ftxt.write("Time(h)\tRin(mV) \tBin(mv) \tRout(mV) \tBout(mV)\r\n")
219 with open((file_net+'Peak2peak.txt'), 'w') as ftxt:
220     ftxt.write("Time(h)\tRin(mV) \tBin(mv) \tRout(mV) \tBout(mV)\r\n")
221
222 ## Main Sensing Infinite Loop ##
223 while True:

```

```

224 #for iterrrr in range(1): #Limited measurement instead of infinite loop
225     if (int((time.time()-time_start)/60) % 10) < 2: # Measure every 10 minutes since
start; allow range of 10 <= time < 12
226         # Total measurement time should be ~2.7 minutes
227         for lasers in range(len(LD_pin)): # Sample from all 4 lasers
228             PDhigh = 0
229             PDlow = 0
230             RPIO.output(LD_pin[lasers], 1) # Begin using this laser
231             time_str = strftime("%Y_%m_%d_%H_%M_%S") #new file with timestamp
232             for i in range(num_pulses*2): # Do this many pulses to average over
233                 if not i%2:#RPIO.input(LD_pin[lasers]):
234                     RPIO.output(LD_pin[lasers], 1) # turn on LD if it is off
235                     #pidList[lasers].set(power[lasers])
236                 else:
237                     RPIO.output(LD_pin[lasers],0)
238                     #pidList[lasers].set(0)
239                 for j in range(5):
240                     try:
241                         time.sleep(0.2) # sleep for 0.2s, 5Hz sampling
242                         with ADClock:
243                             # PD[0] is for input side, PD[1] is for output side
244                             PDvolt = readadc(PD_chan[int(lasers/2)])*3300/1023.0
245                             LDPDvolt = readadc(LDPD_chan[lasers])*3300/1023.0
246                             if RPIO.input(LD_pin[lasers]):
247                                 PDhigh += PDvolt
248                             else:
249                                 PDlow += PDvolt
250                             time_now = (time.time() - time_start)/3600
251                             with open((file_loc+time_str+file_name[lasers]),"a") as ftxt:
252                                 ftxt.write("%f\t%.1f\t%.3f\t%.2f\r\n" %(time_now,
constP.PIDdc[lasers], PDvolt, LDPDvolt))
253                                 with open((file_net+time_str+file_name[lasers]),"a") as ftxt:
254
255 ftxt.write("%f\t%.1f\t%.3f\t%.2f\r\n" %(time_now, constP.PIDdc[lasers], PDvolt, LDPDvolt))
255                 except KeyboardInterrupt): # Stop threads and cleanup
256                     print('Stopping...')
257                     for i in range(len(LD_pin)):
258                         RPIO.output(LD_pin[i], 0)
259                     constP.stop() # End constant checking of laser power
260                     constP.join() # Wait for thread to end
261                     spi.close() # End SPI interface
262                     p.stop() # Clear PWM channel used for pulses
263                     PWM.cleanup() # Clean PWM controller/pins
264                     RPIO.cleanup() # Clean up GPIO pins
265                     print('Stopped.')
266                     raise
267
268             RPIO.output(LD_pin[lasers], 0) # Finish using this laser
269             # Rudimentary peak to peak calculation
270             p_to_p[lasers] = (PDhigh-PDlow)/5.0/num_pulses # 5 samples per pulse with
'num_pulses' number of pulses
271             time.sleep(5) # wait a bit between lasers
272
273             # Done collecting sensor data, write peak to peak to file
274             time_now = time.time() - time_start
275             time_now /= 3600 # convert time to hours elapsed
276             with open((file_loc+'Peak2peak.txt'),'a') as ftxt:
277                 ftxt.write('%.2f\t%.5f\t%.5f\t%.5f\t%.5f\r\n' %(time_now, p_to_p[0],
p_to_p[1], p_to_p[2], p_to_p[3]))
278             with open((file_net+'Peak2peak.txt'),'a') as ftxt:
279                 ftxt.write('%.2f\t%.5f\t%.5f\t%.5f\t%.5f\r\n' %(time_now,
p_to_p[0], p_to_p[1], p_to_p[2], p_to_p[3]))
280             print("Measured one cycle of lasers.")
281         else:
282             try:
283                 time.sleep(30) # wait for some time (?) until checking for measurement time
again
284             except KeyboardInterrupt): # Stop threads and cleanup
285                 print('Stopping...')
286                 for i in range(len(LD_pin)):
287                     RPIO.output(LD_pin[i], 0)

```

```

288         constP.stop() # End constant checking of laser power
289         constP.join() # Wait for thread to end
290         spi.close() # End SPI interface
291         p.stop() # Clear PWM channel used for pulses
292         PWM.cleanup() # Clean PWM controller/pins
293         RPIO.cleanup() # Clean up GPIO pins
294         print('Stopped.')
295         raise
296
297     print('Stopping...')
298     for i in range(len(LD_pin)):
299         RPIO.output(LD_pin[i], 0)
300     constP.stop() # End constant checking of laser power
301     constP.join() # Wait for thread to end
302     spi.close() # End SPI interface
303     p.stop() # Clear PWM channel used for pulses
304     PWM.cleanup() # Clean PWM controller/pins
305     RPIO.cleanup() # Clean up GPIO pins
306     print('Stopped.')

```